

Petrochronology and hydrochronology of tectono-metamorphic events

Valérie Bosse (1), Igor M. Villa (2)

(1) Laboratoire Magmas et Volcans, Université Clermont Auvergne, CNRS, IRD, OPGC, F-63000 Clermont-Ferrand, France; V.Bosse@opgg.univ-bpclermont.fr

(2) Institut für Geologie, Universität Bern, Baltzerstrasse 3, 3012 Bern, Switzerland; Centro Universitario Datazioni e Archeometria, Università di Milano Bicocca, pza della Scienza 4, 20126 Milano, Italy

Abstract

U-Th-Pb petrochronology is based on the incontrovertible fact that the diffusion of radiogenic Pb is negligibly small relative to retrograde reaction rates. Multi-element maps demonstrate that patchy textures tightly correspond to (U+Th)-Pb age variations, requiring that fluid-induced dissolution/ reprecipitation is the principal cause of Pb mobility. Attempts to model intracrystalline core-rim Pb zonation as diffusive transport are not legitimate unless genuine bell-shaped diffusion profiles in minerals can be documented, which happens only exceptionally. Monazite and zircon intra-grain age maps confirm that coupled dissolution-reprecipitation and retrogression reactions assisted by fluids control (Th+U)-Pb ages, not temperature. The chemical zonation observed in many (Th+U)-bearing mineral chronometers (e.g. monazite, allanite, xenotime, zircon) provide petrological constraints. Linking petrology with textures and the isotope record allows reconstructing entire segments of the *P-T-A-X-D-t* history of a rock and its geodynamic environment.

The dearth of mathematically sound diffusion profiles equally applies to the isotope record of micas and feldspars. The tight link between petrology, microtextures, chemical composition and geochronology also pertains to Rb-Sr and K-Ar. Overdetermined multi-mineral Rb-Sr isochrons with excess scatter, and spatially resolved/stepwise release ^{39}Ar - ^{40}Ar results, demonstrate ubiquitous correspondence between relict phases and isotopic inheritance. Many rock-forming minerals are highly retentive of Sr and Ar, unless they are obliterated by retrograde reactions. The rates of dissolution in fluid-controlled reactions are several orders of magnitude faster at upper and mid-crustal levels than diffusive reequilibration rates. Thus, as a rule Rb-Sr and K-Ar chronometers date their own formation.

Accurately establishing *P-T* paths of monometamorphic rocks requires assessing petrologic equilibrium using multivariate thermodynamic software. Dating complex parageneses of polymetamorphic, unequilibrated rocks requires labor-intensive disentangling by: (i) qualitative identification of relicts, retrogression reactions, and chemically open systems by imaging techniques (e.g. cathodoluminescence, element maps, etc.); (ii) microchemical analyses at the μm -scale quantifying heterochemical disequilibrium phases and assigning them to a *P-T-A-X* segment; (iii) spatially resolved/stepwise release, relating the chemical signature of the analyzed mineral to its age. K-Ar and Rb-Sr usually provide a different perspective on the *P-T* evolution of a rock than does (Th+U)-Pb, as K+Rb-rich minerals (phyllosilicates and especially feldspars) mostly form later and react/dissolve faster in the retrograde path than U-rich accessory phases (e.g. Mukai et al., 2014). The present

38 paper reviews these general principles by means of well-understood examples, both successful and
39 unsuccessful in matching the independently known external constraints.

40

41

Introduction

42

43 Geodynamic models of the lithosphere seek to reconstruct the tectonic evolution and its duration. To this end,
44 it is very useful to be able to link the information provided by microstructures to the petrogenesis of that same
45 rock, and to connect both to the time information, to constrain the rates of crustal processes (Vance et al.,
46 2003). The discipline connecting petrology and geochronology was later termed petrochronology (Kylander-
47 Clark et al., 2013). Most metamorphic rocks record not just an instantaneous formation but a plurality of
48 mineral-forming events, such that polymetamorphic and polycyclic rocks predominate in Pre-Cenozoic
49 terrains. When studying Precambrian tectonics, field relations are often obscured by subsequent deformation,
50 and petrological relations are often obscured by multiple metamorphic overprints. This makes tectonic models
51 of Precambrian terrains especially vulnerable to the complexities of mineral geochronometers. The observation
52 of relict minerals with abrupt compositional zonations, and in general of petrologic disequilibrium, poses a
53 fundamental interpretive difficulty: assigning an age to each mineral generation, and linking each generation to
54 the tectonic event that created the metamorphic conditions that led to its growth. Getting analytical data has
55 become apparently easy. It is therefore important to improve the way that a mass spectrometric number is
56 converted into a geological history and geodynamic context. This requires clarifying the approach used to
57 interpret the geochronological data in order to increase the accuracy and reliability of tectonic models based on
58 them.

59 A mineral is a useful petrochronometer if it fulfills two conditions: (1) its composition must be
60 variable, in such a way that it records variable *P-T-A-X-D* (pressure-temperature-water activity-composition-
61 deformation) conditions and allows tracing of chemically open-system behaviour; (2) its petrologic signature
62 and its chronometry must be set simultaneously in the same geological event and remain unmodified ever
63 since. When both conditions are fulfilled, it becomes possible to link the petrological and structural evolution
64 of the chronometer to that of the rock, then on a larger scale to that of the geological unit, and finally to that of
65 the orogenic belt.

66 The present review will discuss the kind of tectonic information that can be gained from
67 geochronological data. To do so, it will address the fundamental assumptions underlying petrochronology by
68 discussing examples of (Th+U)-Pb dating in monazite and K-Ar dating in micas in various tectono-
69 metamorphic contexts. The studied examples show that (i) fluid assisted dissolution-precipitation processes
70 rather than temperature-dependent solid diffusion predominantly govern the closure of the (Th+U)-Pb system;
71 (ii) monazite is particularly sensitive to the interaction with fluids of specific composition (F, CO₂, K ...), even
72 at low temperature; (iii) in the absence of fluids, monazite is able to record HT events and to retain this
73 information during (poly-)metamorphism and even partial melting; (iv) patchy chemical and isotopic
74 zonations, well known in monazite, reflect the fluid-assisted interaction with the surrounding mineral
75 assemblages.

76 K-Ar chronometer minerals show similar patterns of isotopic inheritance closely tied to relict patches
77 and heterochemical retrogression phases (Villa and Williams 2013). Isotopic closure in both (U + Th)-Pb and
78 K-Ar systems follows the same principle: thermal diffusion is very slow, dissolution and reprecipitation are
79 several orders of magnitude faster under typical crustal conditions. This means that both (Th+U)-Pb and K-Ar
80 mineral chronometers are hygrochronometers. The petrochronological interpretation of the ages of the
81 different domains cannot be decoupled from the geochemical and petrological context.

82 One crucial criterium for petrochronology are the relative rates of mineral-forming reactions and of
83 diffusive reequilibration. A mineral that preserves both its major element composition and its radiogenic
84 isotope signature has a petrogenetic stability field that allows its growth at temperatures lower than its "closure
85 temperature" for diffusive loss of radiogenic isotopes as defined by Dodson (1973). Mineral
86 petrochronometers all have this property (they were called "Class II chronometers" by Villa, 2016). In
87 contrast, "Class I chronometers" (also called thermochronometers) are minerals that are open to diffusive loss
88 of one or more daughter isotopes whenever they are formed, and only become closed to diffusive loss at a
89 lower T than that at which they were formed.

90 The focus on petrology also implies, following Villa (1998, 2016), that the ages measured in
91 petrochronometers from metamorphic rocks do not exclusively conform, in a mathematically invertible way,
92 to the "closure temperature" concept (Dodson 1973). Examples of geodynamic models that only focus on the
93 km-to-Mm scale and fail to take into account the atomic scale processes will also be discussed below. The
94 only way forward is to bridge the gap between (sub-)µm-scale processes well understood by petrologists and
95 mineralogists and km-scale processes addressed by tectonic models.

96
97

98 **(Th+U)-Pb petrochronometry**

99

100 Most Th±U-bearing minerals have high field strength elements (HFSE) as major cations, and
101 inherently fulfill the requirement of efficient resistance to retrogradation and consequent degradation of the P -
102 T - A - X information. One such mineral is monazite (Th, U, Ca, Y, Si, LREEPO₄), an accessory mineral in
103 magmatic (mainly peraluminous and carbonatitic) and metamorphic rocks (mainly Ca-poor and Al-rich
104 metapelites) where it represents one of the major reservoirs of lanthanides and actinides in the continental
105 crust (Bea et al. 1996). Because of its wide range of possible cation substitution, monazite is a good tracer of
106 the petrological events. Changes in the concentrations of Y, REE, Th, U reflect the partition of these elements
107 between monazite and other minerals of the paragenesis that was in equilibrium at the time of monazite
108 growth. Thermodynamic modelling allows to place monazite in a P - T - A - X grid (Mottram et al. 2014; Didier et
109 al. 2015). However, integrating monazite in phase relations models and thermodynamic calculations is
110 complex, because thermodynamic models remain highly dependent on the precise measurement of the trace
111 elements in all the associated silicates.

112 Its high Th content (ThO₂ up to 15 wt% and more), and to a lesser extent U (UO₂ content < 2 wt%),
113 allows the simultaneous use of three isotopic ratios (in order of abundance: ²⁰⁸Pb / ²³²Th, ²⁰⁶Pb / ²³⁸U, and ²⁰⁷Pb

114 / ^{235}U) as independent radiometric clocks that control each other. In young (< 50 Ma) and/or U-poor monazite,
115 ^{232}Th – ^{208}Pb ages are preferentially used for two reasons: (i) Th is more abundant than U; (ii) the U decay series
116 could be affected by secular disequilibrium and contain parentless ^{230}Th (Schärer, 1984), resulting in ^{206}Pb excess
117 and overestimated $^{206}\text{Pb}/^{238}\text{U}$ ages. Contrary to zircon, monazite is not sensitive to radiation damage (Seydoux-
118 Guillaume et al., 2002a; Seydoux-Guillaume et al., 2004; Seydoux-Guillaume et al. 2018): despite the high
119 irradiation doses accumulated over long periods due to high Th and U contents, monazite is not affected by
120 amorphisation over time. Thus, the possibility that radiogenic Pb (hereafter Pb*) is lost by leaching from an
121 amorphous crystalline lattice, and the consequent perturbation of the measured ages, can be usually ruled out.
122 Experimental studies (Cherniak et al. 2004 ; Gardés et al. 2006) have shown that intracrystalline volume
123 diffusion of Pb^{2+} in pristine monazite is extremely slow in the laboratory (Fig. 1). In lithospheric conditions it
124 is orders of magnitude slower, as natural Pb* has valence 4+ (Kramers et al., 2009) and therefore has a lower
125 diffusivity (see also below). Thus, neither Pb* diffusion nor Pb* loss caused by radiation damage can disturb
126 the (Th+U)-Pb isotope system. Incorporation of initial unradiogenic ("common") Pb in the crystal structure of
127 monazite was thought to be negligible compared to Pb* (Parrish, 1990). This has encouraged the development
128 of electron microprobe (EMP) dating, whose underlying assumption is that Pb is exclusively of radiogenic
129 origin (Montel et al., 1996; Cocherie et al. 1998; Williams et al. 1999 ; Williams et al. 2011). This is a
130 reasonable assumption in Archean rocks analyzed in these early studies. However, recent experimental
131 (Seydoux-Guillaume et al, 2002b) and natural studies (Janots et al. 2012; Didier et al. 2013) observed
132 incorporation of initial Pb in monazite. Unradiogenic Pb is usually not incorporated in the monazite structure
133 but rather concentrated in nanometer-scale Pb-rich clusters as revealed by transmission electronic microscopy
134 and atom-probe imaging (Seydoux-Guillaume et al. 2003; Fougereuse et al. 2018).

135 In addition to the high retentivity of Pb* at practically all metamorphic temperatures (Cherniak et al.
136 2004; Gardés et al. 2006), monazite has been observed to be very prone to metamorphic recrystallization in the
137 presence of an aqueous fluid (Williams et al. 2007; Villa & Williams 2013; Williams et al. 2017). This
138 manifests itself as variable chemical compositions at the grain scale and complex compositional zoning
139 usually defining intragrain patches of varied size (Williams et al. 1999; Seydoux-Guillaume et al. 2003) and
140 sharp boundaries (Fig. 2 a, b). Such domains recording changes in physical and chemical parameters are
141 usually connected to specific metamorphic stages recorded by the host rock. When chemical variations are
142 related to isotopic variations, it is then possible to distinguish different stages in the petrological evolution of
143 the host rock and then to its geodynamic history (e.g. Manzotti et al. 2018). Each different, coexisting
144 monazite generations records a point in the *P-T-A-X-D-t* path of a rock, disentangling its polymetamorphic
145 evolution. The key point, which will be a red thread throughout this paper, is that the diffusive loss of Pb*
146 from monazite is much slower than that of the major elements of the major minerals that are used to constrain
147 metamorphic *P-T-A-X* conditions. The chemical composition *X* is being adjusted, as the structure-forming
148 elements of the metamorphic paragenesis are still mobile, at a time when the retention of radiogenic daughters
149 in monazite has been complete for quite a while. Therefore, monazite is a "Class II chronometer", and dates its
150 own formation.

151

152

153

Example 1. Monazite thermochronometry: the relevance of diffusion

154

155 Some workers (Steck & Hunziker 1994; Kohn 2013) have instead used monazite as a
156 thermochronometer. The principal criterion to discriminate the legitimacy of this approach is the self-
157 consistency of results, i.e. the modelling of a tectonic history that can be supported by geological arguments,
158 independently of any circular argumentation based on isotopic data.

159

160 Steck and Hunziker (1994) compiled several dozen monazite and mica age data in a transect across the
161 Central Alps. This is a very well mapped area, in which all the "canonical" calibrations of the "closure
162 temperature" approach (Jäger 1967) were based. Steck and Hunziker (1994, their fig. 12) started from the
163 assumption that all mica ages are "cooling ages". From this assumption, a chain of correctly applied logical
164 implications implied two testable predictions: that the age of orogen-wide metamorphism was 38 Ma (the so-
165 called "Lepontine metamorphism"), and that the "closure temperature" of monazite for Pb loss was 450 °C.
166 The key argument for the latter estimate was the ubiquitous finding that $t_B < t_M < t_W$, t_B being the biotite K-Ar
167 age, t_M the monazite U-Pb age and t_W the muscovite-whole rock Rb-Sr age (Fig. 3a). As monazite ages were
168 younger than 38 Ma, their argument was apparently rounded off. However, the subsequent direct
169 determination of Pb diffusivity in monazite (Cherniak et al., 2004; Gardés et al., 2006) established that
170 monazite retains all of its radiogenic Pb* below 800 °C. This meant that all monazite ages in the Central Alps
171 date the (diachronous) peak metamorphism, whose peak T did not exceed 650 °C, to the interval 15-25 Ma
172 (Fig. 3b). The chain of arguments ought to be reversed: since t_W dates the metamorphic peak, any age higher
173 than t_W contains a component of isotopic inheritance and must not be viewed as a "cooling age", negating the
174 validity of the starting assumption. Inheritance affects most muscovite ages and a few biotite ages in an
175 irregular geographic distribution, sometimes varying in the same locality (Arnold and Jäger 1965). The next
176 implication is thus that retention of radiogenic ^{87}Sr and ^{40}Ar (hereafter $^{87}\text{Sr}^*$ and $^{40}\text{Ar}^*$) in relict micas can
177 occur at 600 °C. This has a further corollary: as the thermal retentivity of micas is high, it is necessary to
178 explain the rejuvenation of some (but not all) micas in the same, low thermal conditions by the predominance
179 of a local, sample-dependent process: fluid-assisted recrystallization instead of temperature-controlled
180 diffusion. Indeed, subsequent studies (e.g. Tartèse et al., 2011) document a tight parallelism between monazite
181 and white mica ages, which can only be explained by interaction with aqueous fluids (see below).

181

182 The large-scale tectonic implications are a complete negation of the conclusions by Steck and
183 Hunziker (1994). The metamorphic peak was not synchronous but diachronous in the different units. The
184 relative movement of the units that are now juxtaposed in outcrop in the Central Alps persisted until later than
185 15 Ma. The average exhumation rate from peak pressure to outcrop is doubled. The cause for such a massive
186 misinterpretation of Alpine tectonics was the assumption that monazite and micas were ideal
187 thermochronometers. The assumed "closure temperature" of micas was (unrealistically) low, as in their
188 samples it reflects not diffusion in a chemically closed environment but instead resetting by fluids at very low
189 temperature. One extreme example of dating "white mica" in a petrologically careless/careful way is given by
190 the muscovite-sericite reaction described by Maineri et al. (2003). These workers observed that white mica in

190 a related rock suite could come in two varieties: magmatic muscovite, aged 8.5 Ma; and sericite, reset at 7 Ma
191 at a well-constrained temperature of 230 °C. If they had extrapolated the latter T-t point as a
192 "thermochronological anchor point" of general validity for all white micas, regardless of their petrological
193 origin, they would have estimated a "closure temperature" for white mica similar to, but slightly lower than,
194 that proposed by Jäger (1967). Instead, by paying attention to the mineralogical reactions involving an
195 aqueous fluid they were able to infer the correct sequence of events for Elba Island. In summary, the incorrect
196 assumption that all mineral ages can be inverted to constrain a point in T-t space is bound to give incorrect
197 tectonic reconstructions and unsubstantiated models of orogenic processes.

198 The discussion of the preceding example raises the question which, if any, mineral is a reliable
199 thermochronometer, i.e. one in which the age is always controlled exclusively by diffusion, in such a way that
200 age is always an invertible function of temperature. Diffusion is a very slow process, whose importance in
201 natural rocks has been vastly overrated in the past (cf. the discussion by Villa and Hanchar, 2017, and the
202 many references therein). The requirement stated in the Introduction, that the *P-T-A-X* signature and the
203 isotopic age of a mineral should pertain to the same geological event, amounts to requiring that the diffusivity
204 of the major elements (those on which the thermobarometry is based) must not be smaller than that of the
205 radiogenic isotope that defines the age.

206 The mathematical equations for Fick's Law diffusion have a very simple outcome: diffusion always
207 and only produces a bell-shaped (so-called error function, or erf) spatial concentration profile of the diffusant.
208 If a genuine erf profile is observed, then probably Fickian diffusion was the predominant physical
209 phenomenon in that sample (within the uncertainty of the fit of the data to the erf profile). If the spatial
210 distribution of the diffusant resolvably deviates from an erf profile, then Fickian diffusion was not the
211 predominant physical phenomenon, and numerical inversion models that assume Fickian diffusion are
212 inaccurate and illegitimate.

213 The prime tool for the assessment of core-rim gradients in natural samples is by in-situ dating. In
214 principle, in-situ techniques allow dating a mineral in its petrological-microstructural environment. In practice,
215 an essential limit is the spatial resolution of in-situ analyses. There are two strict physical limits to the
216 accuracy of an in-situ analysis. The upper limit of a useful primary beam diameter is given by the necessity to
217 resolve the intergrowths of diachronous mineral generations in a complete way (Villa & Hanchar 2017, their
218 figure 9). The literature abounds with reports that infer an incorrect age due to the uncorrected mixing of more
219 than one mineral generation. The lower limit of a useful primary beam diameter is given by the necessity to
220 average away the nm-scale recoil of radiogenic daughter nuclides by natural disintegration of the parent
221 nuclide. Such atom-scale phenomena were documented in zircon by Kusiak et al. (2013), Valley et al. (2014)
222 and Whitehouse et al. (2017) and in monazite by Seydoux-Guillaume et al. (2003) and Fougereuse et al.
223 (2018), and result in a local disproportionation of parent and daughter nuclides. An unquestioning, context-
224 less application of a single spot age obtained with a $< 1 \mu\text{m}$ primary beam would cause an incorrect age
225 assignment of an entire orogenic cycle.

226 Studying older rocks by in-situ analyses has advantages and drawbacks. The advantage is that the
227 number of radiogenic atoms that are required for precise dating is contained in a smaller volume. This allows

228 analyses with a higher spatial resolution and thus makes the dating of microstructurally distinct spots less
229 difficult. The drawback is that the time-resolution provided by older rocks is less detailed than that of recent
230 ones. A 1 % age uncertainty on a mid-Archean age, 30 Ma, is the duration of the entire Himalayan orogeny.
231 Using in-situ analyses to tell apart events that lie 1 Ma apart is a serious challenge: for old rocks the analytical
232 precision may be insufficient, for young rocks the spatial resolution may be insufficient to target only one
233 generation of the petrochronometer mineral. Moreover, minor isotopes and/or trace elements are frequently
234 below detection limit if the ablated volume is excessively small. This makes chemical fingerprinting of
235 polyphase mixtures and heterochemical intergrowths difficult or impossible.

236 The disambiguation of mathematically correct erf profiles from generic core-rim zonation, such as e.g.
237 accretion of a discrete heterochemical phase onto a relict core, requires a spatial resolution one or two orders
238 of magnitude better than the length scale of the zonation. Moreover, if one element exhibits a genuine
239 diffusion gradient in a mineral, then all elements whose boundary conditions allow it must exhibit one as well.
240 Since the diffusion length is proportional to \sqrt{Dt} , where D is the diffusion constant and t is the duration of the
241 heating event, all diffusing elements from the same mineral grain must necessarily exhibit diffusion length
242 scales that depend on the (well predictable) relative diffusion coefficients.

243 Neglecting the systematic dependence of diffusivity on charge and radius is not just an academic
244 detail, as it can lead to unrealistic tectonic modelling. As an example, Ewing (2017) used Zr-in-rutile
245 thermometry to determine metamorphic peak temperatures of ca. 850-950 °C in lower crustal granulites from
246 Corsica (France). They then dated the rutile by U-Pb and assumed that their age, 160 Ma, was a "cooling age"
247 corresponding to exhumation of the rutile through the 550-650 °C isotherm. This was interpreted as evidence
248 of the exhumation of the lower crust during the formation of the first oceanic crust in the Late Jurassic.
249 However, a few independent constraints conflict with this tectonic model. Firstly, the Jurassic evolution of the
250 geotherms in the entire Corsica-Sardinia block is constrained by fission tracks and U*-He ages (Malusà et al.
251 2016), whereby the oceanic crust was already being thrust over the continent ca. 10 Ma earlier. Secondly, the
252 lower crust had already been exhumed during the Permian; during the Jurassic rifting the thermal perturbation
253 was weak (Malusà et al 2016). The misunderstanding of diffusion systematics by Ewing (2017) was subtle.
254 The Zr-in-rutile thermometer was assumed to reliably record the peak temperature, which means that the Zr
255 concentration was not modified by diffusive re-equilibration. ~~On the contrary,~~ The ionic radii of Zr⁴⁺ (86 pm)
256 and Pb⁴⁺ (91.5 pm) predict that Pb* diffuses much less fast than Zr, i.e., if Zr-in-rutile records a formation
257 temperature then the U-Pb age of rutile must a fortiori record a formation age.

258 A multichronometric assessment of the internal consistency of models that interpret mica ages
259 following thermochronology was recently reported by Airaghi et al. (2018). Biotite and allanite grew
260 synchronously during burial, and both chronometers give mutually concordant ages between 220 and 180 Ma.
261 The chronometric information recorded by both minerals survived metamorphic peak temperatures of c. 580
262 °C. Retrograde muscovite formed around 130 Ma at c. 370-470 °C (whereby the size mismatch, discussed
263 above, between "small" mineral grains and "large" laser beam prevents reproducible dating of separate
264 muscovite generations: Airaghi et al., 2018, p. 947). Diffusion modelling is unable to reproduce any of these
265 observations (Airaghi et al., 2018, p. 954), as predicted by Villa (2016, p. 8). What the allanite and mica

266 multichronometry really means is that "petrological and microstructural processes prevail over thermally
267 driven diffusion even at high temperatures" (Airaghi et al., 2018, p. 954), which puts new, robust constraints
268 on the Triassic-Jurassic tectonics of the Longmenshan orogen.

269 In a very recent paper, Kirkland et al. (2018) analyzed compositional and Pb isotopic profiles in
270 apatite. They concluded that "To apply Pb diffusion profiles to determine cooling histories, one must not
271 assume but demonstrate that thermally activated volume diffusion is justifiable because our results show that
272 apatite generally may not record simple thermally activated Pb diffusion profiles but rather profiles modified
273 in part or whole by recrystallization or new growth" (Kirkland et al., 2018, p. 155).

274 As evidenced by the three just cited 2017-2018 papers, observations of erf profiles in natural
275 geological systems are very rare (confirming the references cited by Villa 2016). More frequent are the
276 observations of "slow" diffusion being overtaken by superimposed faster processes, such as
277 dissolution/reprecipitation in aqueous fluids (e.g. Labotka et al. 2004, their Fig. 4). The relative magnitude of
278 the rate constants of diffusion and of dissolution also affects very heavily the literature estimates of the
279 geochronology of micas and feldspars. The discussion by Villa (2016) needs not be repeated here; the
280 observation most relevant for the present discussion is that, in the absence of dissolution/reprecipitation due to
281 aqueous fluids, the "dry" diffusivity of the radiogenic daughters in micas ($^{40}\text{Ar}^*$ and $^{87}\text{Sr}^*$) is sufficiently low
282 to make these minerals Class II geochronometers.

283

284

285 **Beyond (Th+U)-Pb: Rb-Sr and K-Ar**

286

287 The reasons why micas are petrochronometers in the Rb-Sr and K-Ar systems must be sought at the atomic
288 scale. Ar is a very large atom (its van der Waals radius $r_{\text{Ar}} = 188$ pm, much larger than oxygen and the
289 structure-forming cations) with a high polarizability. It does not form true bonds but can be adsorbed onto a
290 surface by van der Waals forces, with an activation energy around 10 kJ/mol. Sr^{2+} is even larger and less
291 adapted to the silicate framework (its covalent radius $r_{\text{Sr}^{2+}} = 195$ pm). Pb^{4+} is also very large, and due to its
292 high charge (Kramers et al. 2009) it is one of the slowest diffusants.

293 Definitely a single Ar atom is not a "noble gas" in the thermodynamic sense. The properties of a gas are
294 manifested when there are a few millions other free gas atoms, all of whom obey the equations of statistical
295 mechanics. On the other hand, when an individual Ar atom is trapped interstitially within a solid as a single
296 atom it is so impeded in its movement that Boltzmann's Law [$v \sim \sqrt{kT}$] does not apply. The threshold for
297 gaseous behaviour is reached when the mean free path of the atoms at the T of interest is smaller than the size
298 of the cavity it is confined in. This corresponds to a few hundred nm inclusions (depending on the
299 entrapment P and T). When the inclusion's internal overpressure, given by $P=nRT/V$, exceeds the strength of
300 the solid host, can the trapped atoms be released as a gas by decrepitation.

301 Just as evidently, an Ar atom trapped in a solid is not a Fickian diffusant. After decades of confusion, it has
302 become clear that the measured activation energies for Ar transport provide unambiguous constraints on
303 where, how and why an Ar atom can migrate. Ar makes no bonds with structure-forming cations, nor with

304 oxygen, and thus should have a partition coefficient near zero. Other than in (passively trapped) fluid
305 inclusions, ^{40}Ar never comes into a crystal except as the radiogenic daughter, $^{40}\text{Ar}^*$, of a ^{40}K atom that
306 captured one of its 1s electrons. When the excited $^{40}\text{Ar}^*$ isomer decays to the ground state, it emits a gamma
307 photon with an energy of 1.46 MeV. By momentum conservation, the $^{40}\text{Ar}^*$ nucleus recoils by tens of nm,
308 during which movement it probably also undergoes recoil stripping of a few of its electrons. Thus, the $^{40}\text{Ar}^*$
309 ion is no longer located in the same crystallographic location as its parent isotope ^{40}K . Its positively charged
310 state is metastable and the electrical neutrality might be recovered quickly, but no experimental data exist so
311 far.

312 A further argument against the free mobility of rare gases through the mineral structure is the very different
313 diffusivity and activation energy of Ar and Xe. Hetherington and Villa (2007) measured the degassing rate of
314 irradiated celsian, in which neutron-produced ^{39}Ar and ^{131}Xe were measured simultaneously. If both had been
315 free to move, both should exhibit similar activation energies, of the order of the van der Waals binding
316 energy. Instead, the observed activation energy of Ar in celsian was 180 kJ/mol, similar to that of alkali
317 diffusion, whereas the observed activation energy of Xe was 330 kJ/mol, similar to that of Ba diffusion.

318 The energy budget of Ar migration in natural solids is extremely difficult to measure. Mineral chronometers
319 relevant for the K-Ar system are mostly hydrous (amphiboles, micas), feldspars being the anhydrous mineral
320 most widely used as a chronometer. At this time, the reliable estimates of Ar diffusivity in natural mineral
321 chronometers can be counted on the thumbs of one hand. Experiments on hydrous minerals return the
322 dissolution/reprecipitation rate (Villa, 2010, 2016) instead of the Fick's Law diffusivity. Experiments on
323 feldspars (Wartho et al., 1999) can return a true diffusivity only provided the sample is ideally
324 monomineralic. Polyminerale samples return average properties of the sum of all coexisting phases (Chafe
325 et al., 2014). Despite the general unreliability of literature estimates for Ar diffusivity, a few guidelines can
326 orient users through the apparent disorder of the database: (i) diffusion occurs always, but is always the
327 slowest transport mechanism (Villa, 2016; Villa and Hanchar, 2017 and references therein); (ii) the similarity
328 of activation energies for dissimilar diffusants is proof that the limiting factor in diffusion are the properties
329 of the matrix structure, in particular the creation of Schottky vacancies that allow the movement of cations
330 across the structure; (iii) the vast variations in frequency factors, i.e. of the likelihood that a given ion will
331 exploit the newly created Schottky vacancy, are a function of charge and radius of the diffusant: larger ions
332 have lower frequency factors (Chakraborty and Ganguly, 1992), as do ions with a higher charge (Cherniak
333 2006, 2010).

334 The Rb-Sr ages reported in the references quoted by Steck and Hunziker (1994) are affected by an additional
335 problem besides the relative role of diffusion and recrystallization. The cited mica Rb-Sr ages were all two-
336 point mica-whole rock isochrons. Two-point isochrons may assign a not entirely incorrect general geological
337 era, but their accuracy relies on the isotopic equilibrium between the two analyzed data points. In the case of
338 a metamorphic system, the whole rock always contains relict phases and retrogression products, which
339 guarantees an incomplete isotopic equilibrium and a questionable accuracy of isochrons. When metamorphic
340 rocks are dated by Rb-Sr it is necessary to obtain overdetermined internal isochrons by analyzing a large
341 number of coexisting minerals. The cogeneticity manifests itself by a low dispersion of the data points,

342 whereas rocks showing disequilibrium between relict phases and retrograde minerals also show higher
343 dispersion (e.g. Glodny et al., 2008, their Fig. 5).

344 Reliable laboratory determinations of diffusivity for K-Ar and Rb-Sr mineral geochronometers are very rare
345 (Villa 2016). Practically there is only one mineral, K-feldspar, for which both Sr and Ar diffusion have been
346 determined directly by depth profiling (Ar: Wartho et al. 1999; Sr: Cherniak and Watson 1992). The
347 comparison of the two data-sets shows that both diffusants have a nearly identical activation energy (see
348 above for the physical reasons for this near-identity). However, diffusivities are not equal, as the frequency
349 factor for Ar diffusion is 4×10^{-4} times larger than that for Sr, following the systematic prediction based on
350 charge and radius. This predicts a large age difference between Rb-Sr and K-Ar ages in purely diffusive
351 alkali-rich thermochronometer minerals. Whenever concordant Rb-Sr and K-Ar ages on the same mineral are
352 observed instead, then diffusion was subordinate to recrystallization, which accelerated (at least) the
353 diffusion of Sr by (at least) a factor 40 000.

354

355

356

3.1 Example 2. Mica petrochronometry

357 As mentioned in the introduction, petrochronometers are minerals that allow the estimate of P - T - A - X - d and
358 simultaneously of t . Some minerals, such as e.g. diamond, conveniently shield inclusions from retrogression;
359 this makes them very indirect thermobarometers, and even if diamond can be successfully dated (Burgess et al.
360 2002), defining diamond a petrochronometer seems questionable.

361 More frequently occurring mineral petrochronometers are micas. In a classic Lepontine locality in the Central
362 Alps, Allaz et al. (2011) studied the P - T - A - X evolution by multivariate thermobarometry. From their data it is
363 possible to reconstruct an entire segment of the P - T - t path (Fig. 4). The metamorphic peak at ca. 18-19 Ma
364 (840 ± 50 MPa, 594 ± 14 °C) is dated by monazite U-Pb ages (Janots et al., 2009). One muscovite, AMo0410,
365 gives a ^{39}Ar - ^{40}Ar age of 18.9 ± 0.8 Ma, indistinguishable from the monazite ages. Muscovite of a sample
366 collected < 0.5 km to the North, AMo0409, grew at lower-grade conditions (660 ± 20 MPa, 573 ± 11 °C) at a
367 slightly later time, 17.9 ± 0.6 Ma. The assemblage of AMo0410 records crossing the paragonite-out boundary,
368 which almost completely consumed the first paragonite generation, Prg-1. The rock was exhumed and cooled,
369 thereby re-entering the paragonite stability field at $P = 380 \pm 20$ MPa, $T = 480 \pm 20$ °C. This caused the
370 growth of a texturally clearly distinct Prg-2 generation, whose ^{39}Ar - ^{40}Ar age, 13.3 ± 2.3 Ma, dates the crossing
371 of the paragonite-in boundary. In contrast, paragonite of sample ALu0603, 5 km NNW of the two AMo
372 samples, was not destabilized and its ^{39}Ar - ^{40}Ar age coincides with the muscovite age.

373 From the white mica ages of AMo0410 it is possible to derive an average cooling and exhumation rate
374 between 18.9 ± 0.8 and 13.3 ± 2.3 Ma. The exhumation by 460 ± 27 MPa in 5.6 ± 2.5 Ma corresponds to
375 roughly 3 mm/a. The cooling by ca. 114 ± 13 °C in the same interval gives a cooling rate of 20 ± 9 °C/Ma. In
376 addition to the direct dating of the P - T segment between 840 MPa and 380 MPa, micas in sample AMo410
377 provided an additional bonus. The identical ^{39}Ar - ^{40}Ar ages of 16.3 ± 0.4 Ma obtained on the two biotite
378 samples AMo0409 and AMo0410 are younger than muscovite growth. Both biotite samples record the sum of
379 two processes: genuine diffusion, and chloritization. The two have not been disentangled in this case. It is very

380 doubtful that there exist 100 % retrogression-free biotites on Earth, as even prime museum specimens display
381 microchemical evidence of violation of stoichiometry, attributed to secondary interaction with fluids
382 (Naumenko-Dèzes et al. 2018). In any case, assuming (purely for the argument's sake) that chloritized biotite
383 AMo0410 was not chloritized but only lost Ar by diffusion, then the biotite ages are cooling ages. By
384 interpolating between the muscovite growth at 18.9 ± 0.8 Ma and the Prg-2 growth at 13.3 ± 2.3 Ma, the
385 biotite ages correspond to a temperature of 542 ± 33 °C. A note of caution is that the retention of Ar by biotite
386 below 550 °C cannot be uncritically extrapolated to all biotites of this planet. It only pertains to moderately
387 retrogressed, undeformed minerals, whose petrologic equilibrium has previously been assessed. As dissolution
388 by aqueous fluids is several orders of magnitude faster than thermally activated volume diffusion (Villa 2016,
389 his Fig. 1), even minute traces of water circulation can effect recrystallization at virtually all temperatures. In
390 the absence of a complete *P-T-A-X* characterization of the entire paragenesis, extrapolation of any "closure
391 temperature" for any Class II mineral is not legitimate.

392 An example of the opposite legitimacies of mica thermochronometry and mica petrochronology is the traverse
393 across the Western Alps studied by Villa et al. (2014). These authors observed that in the westernmost part of
394 the traverse white mica underwent major rejuvenation at ambient temperatures < 300 °C, whereas in the
395 easternmost part white mica retained part of its inherited $^{40}\text{Ar}^*$ during, and all of its $^{40}\text{Ar}^*$ after, the eclogitic
396 peak at $T \approx 600\text{-}630$ °C. This contrasting behaviour is clearly incompatible with one good-for-all "closure
397 temperature" (Fig. 5a). What petrology shows instead is that detrital muscovite in the low-grade, water-rich
398 sediments of the western part was progressively recrystallized to phengite. The coupled eastward increase of
399 pressure and deformation effected an increase of the Si substitution in phengite and a correlated rejuvenation.
400 Once all protolith muscovite was converted to phengite, a further eastward temperature increase had no
401 rejuvenating effect on phengite ages, which stayed constant and concordant with the Lu-Hf garnet ages (Fig.
402 5b).

403 Older literature based on white mica thermochronology attributed eclogitization to the Middle Cretaceous,
404 implying subduction of the Liguro-Piemontese Ocean shortly after its Late Jurassic opening, followed 100 Ma
405 later by a separate greenschist overprint. Instead, mica petrochronology established that eclogitization was
406 Eocene, rapidly followed (within 8-10 Ma) by greenschist retrogression along the same exhumation path,
407 making the entire subduction-collision event both younger (by ca. 80 Ma) and more rapid.

408 A potential complication, isotopic inheritance, can be diagnosed both a priori and a posteriori, as it is closely
409 tied to relict patches and heterochemical retrogression phases (Villa and Williams 2013). In this particular
410 locality it had been avoided by choosing monometamorphic metasediments. When dealing with
411 polymetamorphic rocks, sample selection for petrochronology must be preceded by a very extensive
412 petrological groundwork, paying special attention to (i) the achievement and (ii) the preservation of petrologic
413 equilibrium by the rock's mineral assemblage.

414

415

Hygrochronometry

416

417 In metamorphic reactions, fluid-assisted processes are not the exception, but rather the rule (Putnis
418 2002, 2009; Putnis and John 2010). Fluids play a catalytic role by decreasing the activation energy of a
419 reaction and by promoting the dissolution/precipitation processes and material transport. Even at HT
420 conditions in eclogite and granulite conditions, Putnis and Austrheim (2013) showed that the availability of
421 fluids is an essential condition for the metamorphic reactions to proceed, whereas solid-state reactions only
422 involving volume diffusion are not the dominant mechanism (see also Mukai et al., 2014; Centrella et al.,
423 2016). Finally, these authors question the difference between metasomatism and metamorphism and conclude
424 that there is no fundamental difference between the two processes at the molecular scale: metamorphism
425 involves fluids, albeit at local scale and lower volume. Thus, ~~to~~ dating the fluid circulation events associated
426 with the formation of a metamorphic paragenesis requires the use of hydrochronometers.

427 Monazite is well known for its high reactivity in presence of fluids even at low temperatures
428 (Poitrasson et al. 1996; Teufel and Heinrich 1997; Townsend et al. 2001; Seydoux-Guillaume et al. 2002;
429 Bosse et al. 2009; Harlov and Hetherington 2010; Hetherington et al. 2010; Harlov and Hetherington 2011;
430 Williams et al. 2011; Budzyn et al. 2011; Didier et al. 2013): the dissolution/recrystallization processes
431 ubiquitously observed in metamorphic rocks induce the formation of intra-grain monazite domains of distinct
432 age and chemistry, whatever the thermal conditions. Monazite should therefore be called a hydrochronometer.
433 In fluid-assisted dissolution-precipitation processes, precipitation is usually spatially associated with
434 dissolution along the dissolved interface (Putnis 2002). The newly formed monazite usually crystallizes as a
435 more or less discontinuous overgrowth surrounding the primary crystal (see for example Fig. 8 and 9). This is
436 the result of the often restricted mobility of the monazite major elements and induce porosity development,
437 total or partial preservation of the initial grain shape (pseudomorph) and mixing between successive monazite
438 generations at small scale (<500 nm) (Fig. 6; Grand'Homme et al. 2016). This highlights the heterogeneous
439 character of the monazite at the nanoscale observed by atom probe and TEM imaging (Fougerouse et al. 2018;
440 Grand'Homme et al. 2018), and at the same time confirms the negligibility of diffusive reequilibration.
441 Monazite reactivity mainly depends on the *A-X* of the interacting fluid rather than *P-T* conditions (Seydoux-
442 Guillaume et al., 2002 ; Teufel and Heinrich,1997; Hetherington et al., 2010). Experimental studies show that
443 fluids rich in F, CO₂, Ca, and alkali strongly influence the stability of monazite (Hetherington et al., 2010,
444 Harlov and Hetherington, 2010; Harlov and Hetherington, 2011, Budzyń et al., 2011, Richard et al., 2015) and
445 the mobility of Th, U and Pb. Didier et al. (2013) report Th/U fractionation during hydrothermal processes in
446 presence of F-rich fluids with attending age disturbances. Both Th and unradiogenic Pb were independently
447 enriched in variable proportions in the hydrothermal monazite (Fig. 7). This led, in the case studied, to
448 meaningless ²⁰⁸Pb/²³²Th ages, some becoming older by the effect of excess Pb, and some younger by late-stage
449 incorporation of Th. As the U content remained nearly constant, the ²⁰⁶Pb/²³⁸U ratio also scatters, due to
450 external Pb incorporation. A similar behavior has been described with various fluid composition by Janots et al.
451 (2012), Wawrzenitz et al. (2012) and Grand'Homme et al. (2018).

452 During metamorphic reactions, the fluid composition is mainly controlled by local equilibria and
453 depends on the reactivity of the other major and trace minerals involved in the reactions. Because fluid
454 composition also strongly controls the behavior of the monazite during dissolution/recrystallization processes,

455 it is not possible to predict a priori in which direction the Y, REE, Th, U or Pb content will change. Thus low
456 or high-Y or Th content in monazite domains cannot be used a priori as tracers of specific metamorphic
457 conditions (as proposed by Kohn, 2016) in order to attribute ages measured in the same domain to specific
458 metamorphic stages. *P-T-A-X* conditions must instead be calibrated independently for each metamorphic
459 reaction on a case-by-case basis, using the compositions of monazite and of other reactants. With such
460 extensive work, the monazite can be used as a powerful tracer of the tectono-metamorphic events. The
461 recrystallized domains synchronously record the age and the *A-X* conditions at the time of their formation.
462 This allows precise dating of tectonic or metamorphic, successive or polycyclic events. The following
463 examples illustrate the effectiveness of the monazite hydrochronometer for that purpose.

464

465 **Example 3. Dating deformation**

466

467

468

469 Because of the inherent scale limitations of in-situ techniques, direct dating of microstructures in
470 metamorphic rocks remains a challenge (Williams and Jercinovic, 2002; Wawrzenitz et al. 2012; Dumond et
471 al. 2013; Erickson et al. 2015). Dating of deformation first requires a geochronometer mineral showing
472 microstructural evidence of (re)crystallization following the. Secondly, the chemical composition of the
473 geochronometer must reflect the metamorphic conditions taking place during deformation, taking care to
474 recognize and exclude relict grains or inherited subgrains having crystallized before the deformation event.
475 Last but not least, there is the difficulty of resolving the ages of events that are close in time. The didactically
476 illuminating examples provided by Williams et al. (2011) pertain to the discrete Proterozoic overprint of an
477 Archean rock in the Athabasca granulite terrain (Canada) in a separate orogeny. The next challenge is now
478 constraining the petro-hydrochronological sequence of the prograde and retrograde *P-T-A-X-D-t* segments of a
479 single orogenic cycle in the Meso-Cenozoic as an actualistic tool to better understand Precambrian orogenies.

480 Didier et al. (2014) observed deformation textures in monazite grains and dated the deformation events
481 by coupling monazite geochronology with a detailed petrological and structural study. This study focuses on
482 garnet-kyanite (Grt-Ky) metapelites embedded within two major shear zones of the central part of the
483 Rhodope Metamorphic Complex (Greece, Bulgaria) : the Nestos shear zone (NSZ) in Greece and the Chepelare
484 shear zone (CSZ) in Bulgaria. Samples from both locations have experienced two stages of high temperature
485 metamorphism during Alpine times. The first event involved mid-Mesozoic upper amphibolite - granulite
486 facies « dry » melting. The second event involved mid-Cenozoic lower amphibolite fluid-assisted partial
487 melting. All samples, despite some petrological differences, show microstructural evidence for strong ductile
488 shearing in the presence of fluids. Monazite is abundant as inclusions in garnet and kyanite and in the highly
489 foliated matrix. The matrix grains show strong evidence that at least part of their growth occurred during
490 deformation: i) crystallization channeled along muscovite cleavages (Fig. 8a and e), small satellite grains
491 surrounding larger monazite grains (Fig. 8b), iii) clusters of contiguous small grains possibly replacing an
492 older grain (Fig. 8c) or strings of small monazite grains parallel to the matrix foliation (Fig. 8d). These
493 monazites are commonly associated with rutile (Fig. 8e) and biotite grains which also crystallized along the
494 cleavage planes of the host muscovite (Fig. 8c) or in asymmetric strain shadows around garnets. All these

494 textural characteristics of monazite suggest a syn-deformation fluid-assisted monazite growth. Matrix
495 monazite also displays strong chemical and isotopic zoning : the large Y-poor cores yield mid-Mesozoic ages
496 (ca. 115 and 165 Ma), similar to the monazite inclusions in garnet and kyanite, and the thin, commonly
497 irregular Y-rich rims yield Cenozoic ages (ca. 36 Ma) (Fig. 9). The small Y-rich monazite grains parallel to the
498 main foliation also display Cenozoic ages. These observations clearly show that new syndeformation monazite
499 generation formed at ca. 36 Ma as the result of fluid-assisted inter-grain mass transfer.

500 Mesozoic monazite is the main precursor of the new monazite generation. Hence, a process of
501 dynamic dissolution–reprecipitation, as described by Wawrzenitz et al. (2012), probably accounts for the
502 growth of the Cenozoic monazite: the chemical composition of the new grains record the metamorphic
503 conditions of the new environment during deformation, and the shape of the monazite grains indicates the
504 sense of shear, thus linking the measured ages directly to the map-scale tectonic transport. Sharp boundaries
505 separating the chemical domains of distinct ages testify that old monazite grains survive the intense fluid-
506 assisted deformation and are totally preserved. Diffusion processes were not effective. Clearly, the record of
507 the deformation age is the result of dissolution-recrystallization processes rather than intracrystalline
508 temperature-dependent diffusion of trace elements.

509 In the Rhodope samples, the recrystallization of monazite occurs at $P \approx 8\text{-}10$ kbar and $T \approx 650$ °C. But
510 dissolution – recrystallization of the monazite is also known to be possible at lower grade conditions. In the
511 Variscan Agly massif localized in the North-Pyrenean zone (Eastern Pyrénées, France), Variscan monazite in
512 para- and ortho-gneisses sampled in mylonitic shear zones displays recrystallized domains of Cretaceous age
513 (125-110 Ma) related to the Albian extension between the Iberian and European plates. In these samples, fluid-
514 assisted deformation occurs at decreasing temperature conditions from $T > 550$ °C to $T \approx 200$ °C. Younger ages
515 (c. 110 Ma) are associated with brittle deformation whereas older ages (c. 125 Ma) are associated with ductile
516 microstructures suggesting a continuous record of the deformation during the cooling and the exhumation of
517 the Agly massif in the Cretaceous times (Aumar, 2018). It is important to note that Cretaceous ages have been
518 only recorded in syn-tectonic minerals such as monazite, titanite ((Th+U)-Pb system) and micas (K-Ar
519 system) (Chelalou et al. 2016; Nicolas, 1998), but not in zircon. Outside the shear zones, Variscan monazites
520 are preserved. These examples again document that fluid-assisted recrystallization during deformation is
521 responsible for the isotopic closure of the (U+Th)-Pb and K-Ar systems in minerals that actively participate in
522 metamorphic reactions.

523

524

525 **Example 4. Polyclism and polymetamorphism**

526

527 Crystalline complexes occasionally feature rocks having experienced polycyclic metamorphism during
528 several successive orogenies and/or other geodynamic settings. Polyclism needs to be distinguished from
529 continuous successive stages of a *P-T* path during a single orogenic cycle (Gautier et al. 2017). The possible
530 identification of several stages of deformation or successive metamorphic parageneses may only reflect the
531 complex evolution of a single orogen. Geochronological data may give the best evidence of polyclism,

532 provided that these are closely related to structural and petrological data. In contrast, an erroneous attribution
533 of some ages to structures and/or metamorphic assemblages can lead to a wrong tectonic interpretation. This is
534 especially the case for polycyclism, as specific metamorphic conditions (e.g. eclogitization or migmatization)
535 related to an old orogeny may be attributed to a younger one. However, dating the mineral assemblages
536 corresponding to distinct metamorphic events in the same rock is never easy, especially when *P-T* conditions
537 of these events are close. This is the case for the Grt-Ky metapelites described above (Didier et al., 2014), for
538 which a detailed petrological study did not allow rigorous identification of two Mesozoic and Cenozoic
539 parageneses. Only matrix monazite was able to record the two successive events, thanks to the presence of
540 fluids during the deformation in Cenozoic times.

541 Another example of polycyclism recorded by monazite is given by the study of coronitic paragneisses
542 in the Les Essarts high-pressure unit, which occurs in the Southern Armorican Massif (Vendée, Western
543 France). It delineates a NW–SE-trending zone about 70 km long and a few km wide, between two late-
544 Variscan dextral faults (e.g., Godard, 2001, 2009). It comprises eclogite and amphibolite derived from
545 eclogite, which form lenses several km long, stretched and boudinaged in ortho- and paragneisses. The host
546 coronitic paragneisses have undergone a complex evolution: high-T metamorphism ($T \approx 670 \text{ }^\circ\text{C}$, $P \approx 0.32$
547 GPa) followed by retrogression during Proterozoic times and eclogite-facies overprint ($T \approx 700 \text{ }^\circ\text{C}$, $P \approx 1.6$
548 GPa) and final retrogression during Variscan times (Godard, 2009). The second episode gave rise to many
549 pseudomorphic and coronitic reactions and caused high-pressure minerals to grow at the expense of the
550 previous high-temperature parageneses. Monazite is highly abundant in the coronitic paragneisses. Some
551 samples show disequilibrium textures with the surrounding matrix minerals. Apatite-bearing coronas around
552 monazite only developed at contacts with plagioclase following the reaction : $\text{Mnz1} + \text{Pl} (\text{LP} - \text{HT}) = \text{Mnz2} +$
553 $\text{Ap} + \text{Zo} (\text{HP} - \text{LT})$ (Fig.10a). This gives us the opportunity to date the different metamorphic events in these
554 samples. Very small chemical differences are observed between the core of the M1 monazite grains (c. 30 to
555 $>100 \text{ }\mu\text{m}$ in size) and the small M2 monazite grains in the corona ($< 5\mu\text{m}$ in size). This argues in favour of
556 very limited element transport during the reaction and in situ dissolution/reprecipitation processes. Regarding
557 the geochronological data, three different groups of ages can be distinguished. Few data yield concordant Th-
558 U-Pb ages in the monazite cores at around 590 – 600 Ma, whereas the majority of the measured ages is at
559 around 485 Ma (Fig. 10b; Bosse et al. 2010). The third group corresponds to the M2 monazites in the corona.
560 Because of the small size of the M2 grains relative to the laser spot size (5 μm), which induces a variable
561 amount of mixing with the adjacent minerals and unradiogenic Pb contamination, most of the M2 analyses are
562 discordant. The few concordant ones are highly scattered. Thus constraining the age of the HP event in these
563 samples was not easy mainly for technical reasons (i.e. the laser spot size) and the results are not very precise,
564 between 400 and 350 Ma. The most striking feature here is that, despite the complexity of the petrological
565 context (i.e. the presence of multiple and varied pseudomorphs and coronas), the early monazite retains its
566 primary chemical and isotope characteristics. It only partially recrystallizes via in situ
567 dissolution/reprecipitation during HP metamorphic (possibly dehydration) reactions. In neighbouring samples
568 following the same petrological evolution, when monazite coronas are absent, the HP Variscan event is not

569 recorded by the monazite. This demonstrates that petrological processes governed the closure of isotopic
570 systems in monazite and ages obtained in monazite date its ~~own~~ crystallization.

571 For this reason, monazite is a very good tracer of the petrological processes, unlike zircon, which
572 cannot easily be used as a petrochronometer. As it is usually associated with allanite, apatite or xenotime, with
573 which it shares its constituent elements, monazite exhibits textures that directly reflect the metamorphic
574 reactions. Thus dating successive metamorphic stages following the prograde or retrograde sequence of rare
575 earth minerals along a single polymetamorphic orogenic cycle is quite easy, providing in situ ages in
576 microstructural context. Some nice examples exist in the literature (Janots et al. 2008; Janots et al. 2009;
577 Regis et al. 2014). Skrzypek et al. (2016) provide textural and geochronological arguments to constrain
578 monazite petrogenesis and the age of metamorphic events in medium-grade metasedimentary rocks from the
579 Orlica-Śnieżnik Dome (Czech Republic/Poland). A first monazite generation formed via allanite breakdown
580 during garnet growth at prograde to peak P - T conditions (5–7 kbar, 575–640 °C) at around 360–340 Ma.
581 Retrograde processes are responsible for the dominant monazite age population of 330–310 Ma ascribed to a
582 combination of (1) transient monazite growth after allanite and controlled by P availability, (2) variable
583 recrystallization/ replacement of older monazite grains, and (3) minor monazite neoformation due to the
584 resorption of garnet or apatite. These successive episodes of monazite growth evidence the metamorphic
585 reactions involving major and trace minerals during one single orogenic cycle.

586 If the reactions involving petrochronometers and major phases are well identified and calibrated in
587 terms of P - T - A - X conditions, and only in this case, they can be used to calculate duration or exhumation rates.
588 As a recent example, Manzotti et al. (2018) propose to evaluate the exhumation rate of the Gran Paradiso and
589 Money Units (Western Alps) by studying the relative timing of the growth and dissolution of the accessory
590 phases. Combining thermodynamic modelling with HP inclusion, textural and chemical data from both major
591 and accessory phases, these authors were able to date the metamorphic peak and retrograde evolution by fixing
592 P - T conditions of the crystallization episodes of allanite, monazite and xenotime (Fig. 11). The whole set of
593 petrochronological data allow to constrain an exhumation rate of the order of 2.2–5 mm/a for these HP units.
594 This type of approach gives results that substantially differ from calculations only based on closure
595 temperature estimations. As the P - T signature and chronometry are simultaneously constrained, the results
596 allow much more accurate geodynamic models.

597

598

599

600

Concluding remarks

601

- 602 1. Tectonic models are only as good as the weakest link in the quantification of a P - T - A - X - D - t path.
- 603 2. Texture-oriented, high-resolution petrography discriminates equilibrium parageneses from fluid-infiltrated,
604 retrogressed portions of mineral grains and from relict phases.
- 605 3. Polygenetic assemblages provide petrochronological constraints if both the petrological and the
606 chronological record are pristine. The examples presented of monazite and mica petrochronometry illustrate

607 that intra-grain unequilibrated, patchy heterogeneities of chemical and isotopic compositions record
608 discontinuous growth phenomena (see also Zhu and O'Nions 1990). Retrograde reactions require cation
609 transfer in a chemically open system.

610 4. The diffusivity of the ionic species in dry solids is very slow, and usually does not allow chemical reactions
611 to take place in the absence of fluids. The total absence of fluids is a rare phenomenon in terrestrial rocks.
612 Migration and homogenization of chemical species in rocks are many orders of magnitude faster if they are
613 assisted by fluids, enhanced even more if deformation facilitates the movement of this fluid. The presence of
614 fluids as a free phase at the grain boundaries plays a role of catalyst by decreasing the activation energy
615 necessary for the initiation of a reaction and by promoting the dissolution of the reactants, the ion transport in
616 solution and reprecipitation of products. Even in apparently anhydrous environments such as granulite or
617 eclogite facies all solid-solid pseudomorphose reactions between anhydrous minerals necessarily involve an
618 aqueous fluid phase. This makes all petrochronometer minerals discussed here to hydrochronometers.

619 5. The availability of aqueous fluids and the rejuvenation of mineral ages are linked not only for HFSE-
620 dominated minerals (most (Th+U)-bearing chronometers) but even more so for LILE-dominated minerals
621 (alkali-bearing minerals such as micas and feldspars). Both kinds of minerals are hydrochronometers, but as
622 their susceptibility to aqueous fluids is different, they record different episodes in the *P-T-A-X-D-t* path.

623 6. Segments of a *P-T-A-X-D-t* path can be recorded by prograde/peak/retrograde phases if diffusive re-
624 equilibration was slower than fluid-assisted, coupled dissolution-reprecipitation. This requirement is met by
625 diamond, zircon, monazite, allanite, rutile, micas, and feldspars, all of which should be viewed as bona fide
626 petrochronometers. It is not met by most (Th+U)-He mineral geochronometers, which behave as
627 thermochronometers.

628

629

630

631

References

- 632 Airaghi L., Warren C.J., de Sigoyer J., Lanari P., Magnin V. (2018) Influence of dissolution/reprecipitation reactions
633 on metamorphic greenschist to amphibolite facies mica $^{40}\text{Ar}/^{39}\text{Ar}$ ages in the Longmen Shan (eastern Tibet). J.
634 Metamorph. Geol. 36, 933–958
- 635 Allaz J., Berger A., Engi M. and Villa I.M. (2011) The effects of retrograde reactions and of diffusion on ^{39}Ar - ^{40}Ar
636 ages of micas. Journal of Petrology 52, 691-716
- 637 Arnold A. and Jäger E. (1965) Rb-Sr Altersbestimmungen an Glimmern im Grenzbereich zwischen voralpinen
638 Alterswerten und alpiner Verjüngung der Biotite. Eclogae Geologicae Helvetiae, 58, 369-390.
- 639 Aumar C. (2018) Cinématique, métamorphisme et marqueurs géochronologiques de l'extension crétacée du massif
640 hercynien de l'Agly (Pyrénées orientales). Master Research, Clermont Auvergne University, France.
- 641 Bea F. (1996) Residence of REE, Y, Th and U in granites and crustal protoliths ; implications for the chemistry of
642 crustal melts. J. of Petrol. 37, 521-552.
- 643 Bosse V., Boulvais P., Gautier P., Tiepolo M., Ruffet G., Devidal J.L., Cherneva Z., Gerdjikov I. and Paquette J.L.
644 (2009). Fluid-induced disturbance of the monazite Th-Pb chronometer: in situ dating and element mapping in
645 pegmatites from the Rhodope (Greece, Bulgaria). Chemical Geology, 261, 286–302
- 646 Bosse V., Godard G. and Shea T. (2010) Datations des événements polymétamorphiques : intérêts majeurs de l'analyse
647 in situ par ablation laser dans la monazite (Complexe des Essarts, Vendée) Réunion des sciences de la Terre 2010
648 (Bordeaux, France)
- 649 Budzyn B, Harlov DE, Williams ML, Jercinovic MJ (2011) Experimental determination of stability relations between
650 monazite, fluorapatite, allanite, and REE-epidote as a function of pressure, temperature, and fluid composition. Am
651 Mineral 96:1547–1567
- 652 Burgess R., Layzelle E., Turner G. and Harris J.W. (2002) Constraints on the age and halogen composition of mantle
653 fluids in Siberian coated diamonds. Earth and Planetary Science Letters 197, 193-203

654 Centrella S., Austrheim H., Putnis A. (2016) Mass transfer and trace element redistribution during hydration of
655 granulites in the Bergen Arcs, Norway. *Lithos*, 262, 1-10

656 Chafe A.N., Villa I.M., Hanchar J.M. and Wirth R. (2014) A re-examination of petrogenesis and $^{40}\text{Ar}/^{39}\text{Ar}$ systematics
657 in the the Chain of Ponds K-feldspar: "diffusion domain" archetype versus polyphase hydrochronology.
658 *Contributions to Mineralogy and Petrology* 167(5), paper 1010, 1-17, doi: 10.1007/s00410-014-1010-x

659 Chakraborty S. and Ganguly J. (1992) Cation diffusion in aluminosilicate garnets: experimental determination in
660 spessartine-almandine diffusion couples, evaluation of effective binary diffusion coefficients, and applications.
661 *Contributions to Mineralogy and Petrology*, 111, 74–86

662 Chelalou R., Nalpas T., Bousquet R., Prevost M., Lahfid A., Poujol M., Ringenbach J.-C. and Ballard J.-F. (2016) New
663 Sedimentological, Structural and Paleo-Thermicity Data in the Boucheville Basin (eastern North Pyrenean Zone,
664 France). *Comptes Rendus Géoscience* 348, 312–321.

665 Cherniak, D.J., (2006) Pb and rare earth element diffusion in xenotime. *Lithos* 88, 1–14.

666 Cherniak D.J. (2010) Diffusion in accessory minerals: zircon, titanite, apatite, monazite and xenotime. *Rev Mineral*
667 *Geochem* 72:827–869

668 Cherniak D.J., Watson B.E., Grove M. and Harrison T.M. (2004) Pb diffusion in monazite: a combined RBS/SIMS
669 study. *Geochimica et Cosmochimica Acta* 68, 829–840.

670 Cocherie, A., Legendre, O., Peucat, J.-J., Kouamelan, A.N., 1998. Geochronology of polygenetic monazites constrained
671 by in situ electron microprobe Th-U-total lead determination: implications for lead behavior in monazite. *Geochim.*
672 *Cosmochim. Acta* 62, 2475–2497.

673 Didier A., Bosse V., Boulvais P., Bouloton J., Paquette J.L., Montel J.M. and Devidal J.L. (2013) Disturbance versus
674 preservation of U–Th–Pb ages in monazite during fluid–rock interaction: textural, chemical and isotopic in situ study
675 in microgranites (Velay Dome, France). *Contrib. Mineral. Petrol.* 165, 1051–1072

676 Didier A., Bosse V., Cherneva Z., Gautier P., Georgieva M., Paquette J.L. and Gerdjikov I. (2014). Syn-deformation
677 fluid-assisted growth of monazite during renewed high-grade metamorphism in metapelites of the Central Rhodope
678 (Bulgaria, Greece) *Chemical Geology* 381, 206–222

679 Didier A., Bosse V., Bouloton J., Mostefaoui S., Viala M., Paquette J.L., Devidal J.L., Duhamel R. (2015). NanoSIMS
680 mapping and LA-ICP-MS chemical and U–Th–Pb data in monazite from a xenolith enclosed in andesite (Central
681 Slovakia Volcanic Field). *Contribution to Mineralogy & Petrology* vol.170, p.45, doi:10.1007/s00410-015-1200-1.

682 Dodson, M. H., 1973. Closure temperature in cooling geochronological and petrological systems. *Contr. Miner. Petrol.*,
683 40, 259-274.

684 Dumond G, McLean N, Williams M, Jercinovic M, Bowring S (2008) High-resolution dating of granite petrogenesis
685 and deformation in a lower crustal shear zone: Athabasca granulite terrane, western Canadian Shield. *Chemical*
686 *Geology*, 254:175–196.

687 Erickson T.M., Pearce M.A., Taylor R.J.M., Timms N.E., Clark C., Reddy S.M. and Buick I.S. (2015) Deformed
688 monazite yields high-temperature tectonic ages. *Geology*, 44, 635-638

689 Ewing T.A., Beltrando M., Müntener O. (2017) U–Pb thermochronology of rutile to constrain the exhumation history of
690 the lower crust: an example from Alpine Corsica. Abstracts, Congresso Società Geologica Italiana, p. 377. doi:
691 10.3301/ABSGI/2017.01

692 Fougereuse D., Reddy S.M., Saxey D.W., Erickson T.M., Kirkland C.L., Rickard W.D.A, Seydoux-Guillaume A.M.,
693 Clark C. and Buick I.S. (2018) Nanoscale distribution of Pb in monazite revealed by atom probe microscopy.
694 *Chemical Geology* 479, 251-268. <https://doi.org/10.1016/j.chemgeo.2018.01.020>

695 Gardés E, Jaoul O, Montel JM, Seydoux-Guillaume AM, Wirth R (2006) Pb diffusion in monazite: an experimental
696 study of $\text{Pb}^{2+} + \text{Th}^{4+} \leftrightarrow 2\text{Nd}^{3+}$ interdiffusion. *Geochim. Cosmochim. Acta* 70, 2325-2336.

697 Gautier P. Bosse V. , Cherneva Z., Didier A., Gerdjikov I. And Tiepolo M. (2017). Polycyclic alpine orogeny in the
698 Rhodope Metamorphic Complex: the record in migmatites from the Nestos Shear Zones (N. Greece). *Bull. Soc.*
699 *Géol. France - Earth Sciences Bulletin* 188, 2017, 36 DOI: 10.1051/bsgf/2017195

700 Glodny J., Kühn A., Austrheim H. (2008) Geochronology of fluid-induced eclogite and amphibolite facies metamorphic
701 reactions in a subduction–collision system, Bergen Arcs, Norway. *Contr. Miner. Petrol.*, 156, 27-48

702 Godard G. (2001): The Les Essarts eclogite-bearing metamorphic complex (Vendée, southern Armorican Massif,
703 France): pre-Variscan terrains in the Hercynian belt? *Géol. France*, 2001(1–2), 19–51

704 Godard G. (2009) Two orogenic cycles recorded in eclogite-facies gneiss from the southern Armorican Massif (France)
705 *Eur. J. Mineral.*, 21, 1173–1190

706 Grand'Homme A., Janots E., Seydoux-Guillaume A.M., Guillaume D., Bosse V. and Magnin V. (2016) Partial resetting
707 of the U-Th-Pb systems in experimentally altered monazite: Nanoscale evidence of incomplete
708 replacement. *Geology*, v. 44, p. 431-434

709 Grand'Homme A., Janots E., Seydoux-Guillaume A.M., Guillaume D., Magnin V., Hövelmann J., Höschen C. and
710 Boiron M.C. (2018) Mass transport and fractionation during monazite alteration by anisotropic replacement. *Chem.*
711 *Geol.* 484, 51–68

712 Harlov D. E. and Hetherington C. J. (2010) Partial high-grade alteration of monazite using alkali-bearing fluids:
713 Experiment and nature. *Am. Mineral.* 95:1105-1108.

714 Harlov D. E. and Hetherington C. J. (2011) Fluid-mediated partial alteration in monazite: the role of coupled
715 dissolution–reprecipitation in element redistribution and mass transfer. *Contrib Mineral Petrol* 162:329–348

716 Hetherington C.J., Villa I.M., 2007. Barium silicates of the Berisal Complex, Switzerland: A study in geochronology
717 and rare-gas release systematics. *Geochim. Cosmochim. Acta* 71, 3336-3347.

718 Hetherington CJ, Harlov DE, Budzyn B (2010) Experimental metasomatism of monazite and xenotime: mineral
719 stability, REE mobility and fluid composition. *Contrib. Mineral. Petrol.* 99:165-184.

720 Jäger, E., 1967. Die Bedeutung der Biotit-Alterswerte. In: Rb-Sr Altersbestimmungen an Glimmern der Zentralalpen
721 (Eds E. Jäger, E. Niggli and E. Wenk) *Beitr. Geol. Karte Schweiz, NF*, 134, 28-31.

722 Janots E., Engi M., Berger A., Allaz J., Schwarz J-O. and Spandler C. (2008). Prograde metamorphic sequence of REE
723 minerals in pelitic rocks of the Central Alps: implications for allanite–monazite–xenotime phase relations from 250
724 to 610 °C. *J. Metamorphic Geol.*, 2008, 26, 509–526.

725 Janots E, Engi M, Rubatto D, Berger A., Gregory C, Rahn M (2009) Metamorphic rates in collisional orogeny from in
726 situ allanite and monazite dating. *Geology* 37:11-14.

727 Janots E, Berger A, Gnos E, Whitehouse M, Lewin E, Pettke T (2012) Constraints on fluid evolution during
728 metamorphism from U–Th–Pb systematics in Alpine hydrothermal monazite. *Chem Geol* 326-327:61–71

729 Kirkland C.L., Yakymchuk C. Szilas K., Evans N., Hollis J., McDonald B., Gardiner N.J. (2018) Apatite: a U-Pb
730 thermochronometer or geochronometer? *Lithos*, 318-319, 143-157

731 Kohn M.J. (2013). Geochemical zoning in metamorphic minerals. In: *Treatise on Geochemistry*, v. 3: The Crust (R.
732 Rudnick, ed.). Elsevier, 2nd edition. 249-280.

733 Kohn M.J. (2016) Metamorphic chronology—a tool for all ages: Past achievements and future prospects. *American
734 Mineralogist*, Volume 101, pages 25–42, 2016

735 Kramers J.D., Frei R., Newville M., Kober B., Villa I.M. (2009) On the valency state of radiogenic lead in zircon and
736 its consequences. *Chem. Geol.*, 261, 3-10

737 Kusiak M.A., Whitehouse M.J., Wilde S.A., Nemchin A.A. and Clark C. (2013) Mobilization of radiogenic Pb in zircon
738 revealed by ion imaging: Implications for early Earth geochronology. *geology* v. 41; no. 3; p. 291–294

739 Kylander-Clark A.R.C., Hacker B.R. and Cottle J.M. (2013) Laser-ablation split-stream ICP petrochronology, *Chemical
740 Geology* 345, 99–112

741 Labotka T.C., Cole D.R., Fayek M., Riciputi L.R. and Stadermann F.J. (2004) Coupled cation and oxygen-isotope
742 exchange between alkali feldspar and aqueous chloride solution. *American Mineralogist*, 89, 1822-1825

743 Maineri C., Benvenuti M., Costagliola P., Dini A., Lattanzi P.F., Ruggieri G., Villa I.M. (2003) Alkali-metasomatic
744 processes at La Crocetta raw ceramic material mine (Elba Island, Italy): interplay between magmatism, tectonics and
745 mineralization. *Mineralium Deposita*, 38, 67-86

746 Malusà M.G., Danišik M., Kuhlemann J. (2016) Tracking the Adriatic-slab travel beneath the Tethyan margin of
747 Corsica-Sardinia by low-temperature thermochronometry. *Gondwana Res.* 31, 135-149

748 Manzotti P., Bosse V., Pitra P., Robyr M., Schiavi F. and Balleve M. (2018) Exhumation rates in the Gran Paradiso
749 Massif (Western Alps) constrained by in situ U–Th–Pb dating of accessory phases (monazite, allanite and xenotime).
750 *Contributions to Mineralogy and Petrology* (2018) 173:24 <https://doi.org/10.1007/s00410-018-1452-7>

751 Montel, J.-M., Foret, S., Veschambre, M., Nicollet, C., Provost, A., 1996. Electron microprobe dating of monazite.
752 *Chem. Geol.* 131, 37–53.

753 Mottram C. M, Warren C.J., Regis D., Roberts N.N.W., Harris N.B.W., Argles T.W. and Parrish R.R. (2014)
754 Developing an inverted Barrovian sequence; insights from monazite petrochronology. *Earth Planet. Sci. Lett.* 403,
755 418–431

756 Mukai H., Austrheim H., Putnis C.V., Putnis A. (2014) Textural Evolution of Plagioclase Feldspar across a Shear Zone:
757 Implications for Deformation Mechanism and Rock Strength *J. Petrol.* 55, 1457-1477

758 Naumenko-Dèzes, M.O., Rolland Y., Lanari P., Villa I.M., 2018. Intra-grain chronological and compositional
759 inhomogeneity of magmatic micas. Abstract, AGU Fall Meeting, Washington, December 2018

760 Nicolas R. “Etude Géochronologique et Pétrostructurale Du Massif de l’Agly,” Master research, Montpellier
761 University, France, 1998.

762 Poitrasson F, Chenery S, Bland DJ (1996) Contrasted monazite hydrothermal alteration mechanisms and their
763 geochemical implications. *Earth Planet. Sci. Lett.* 145:79–96.

764 Putnis A (2002) Mineralogical replacement reactions: from macroscopic observations to microscopic mechanisms.
765 *Mineral.Mag.* 66:689-708.

766 Putnis A, (2009) Mineral Replacement Reactions. *Rev. Mineral. Geochemistry* 70, 87–124.

767 Putnis A. and Austrheim H. (2013) Mechanisms of metasomatism and metamorphism on the local mineral scale: the
768 role of dissolution-precipitation during mineral re-equilibration. In: Harlov D.E., Austrheim H. (eds.),
769 *Metasomatism and the Chemical Transformation of Rock*. Springer, Heidelberg, 141-170. ISBN 978-3-642-28393-2.

770 Putnis A. and John, T. (2010) Replacement Processes in the Earth’s Crust. *Elements*, 6, 159-164

771 Regis D., Rubatto D., Darling J., Cenko-Tok B., Zukali M. and Engi M. (2014) Multiple Metamorphic Stages within an
772 Eclogite-facies Terrane (Sesia Zone, Western Alps) Revealed by Th-U-Pb Petrochronology. *J. of Petrol.* 55, 1429-
773 1456

774 Richard A, Montel J-M, Leborgne R, Peiffert C, Cuney M, Cathelineau M (2015) Monazite Alteration in H₂O ± HCl ±
775 NaCl ± CaCl₂ Fluids at 150°C and p_{sat}: Implications for Uranium Deposits. *Minerals* 5:693–706

776 Schärer, U., Hamet, J., Allègre, C.J., 1984. The Transhimalaya (Gangdese) plutonism in the Ladakh region: a U-Pb and
777 Rb-Sr study. *Earth and Planetary Science Letters* 67, 327-339.

778 Seydoux-Guillaume, A.M., Wirth, R., Nasdala, L., Gottschalk, M., Montel, J.M., and Heinrich, W., (2002a), An XRD,
779 TEM and Raman study of experimentally annealed natural monazite: *Physics and Chemistry of Minerals*, v. 29, p.
780 240–253.

781 Seydoux-Guillaume, A.M., Paquette, J.L., Wiedenbeck, M., Montel, J.M., and Heinrich, W., (2002b), Experimental
782 resetting of the U-Th-Pb system in monazite: *Chemical Geology*, v. 191, p. 165–181.

783 Seydoux-Guillaume A.M., Goncalves P., R. Wirth, A. Deutsch (2003) Transmission electron microscope study of
784 polyphase and discordant monazites: Site-specific specimen preparation using the focused ion beam technique
785 *Geology*; v. 31; no. 11; p. 973–976

786 Seydoux-Guillaume A.M., Wirth R., Deutsch A. and Schärer U. (2004) Microstructure of 24-1928 Ma concordant
787 monazites; implications for geochronology and nuclear waste deposits. *Geochimica et Cosmochimica Acta*, Vol. 68,
788 No. 11, pp. 2517–2527

789 Skrzypek E., Bosse V., Kawakami T., Martelat J.E. and Štípská P. (2016) Transient allanite replacement and prograde
790 to retrograde monazite (re)crystallization in medium-grade metasedimentary rocks from the Orlica-Śnieżnik Dome
791 (Czech Republic/Poland): Textural and geochronological arguments. *Chemical Geology*,
792 <http://dx.doi.org/10.1016/j.chemgeo.2016.11.033>

793 Steck A. and Hunziker J. (1994) - The tertiary structural and thermal evolution of the Central Alps – compressional and
794 extensional structures in an orogenic belt. *Tectonophysics*, 238, 229-254.

795 Tartèse R., Ruffet G., Pouchol M., Boulvais P., Ireland T.R. (2011) - Simultaneous resetting of the muscovite K-Ar and
796 monazite U-Pb geochronometers: a story of fluids. *Terra Nova*, 23, 390-398.

797 Teufel S, Heinrich W (1997) Partial resetting of the U–Pb isotope system in monazite through hydrothermal
798 experiments: an SEM and U–Pb isotope study. *Chemical Geology* 137:273–281.

799 Townsend KJ, Miller CF, D'Andrea JL, Ayers JC, Harrison TM and Coath CD (2001) Low temperature replacement of
800 monazite in the Ireteba granite, Southern Nevada: geochronological implications. *Chem Geol* 172:95–112.

801 Valley, J.W., Cavosie, A.J., Ushikubo, T., Reinhard, D.A., Lawrence, D.F., Larson, D.J., Clifton, P.H., Kelly, T.F.,
802 Wilde, S.A., Moser, D.E., Spicuzza, M.J., 2014. Hadean age for a postmagma- ocean zircon confirmed by atom-
803 probe tomography. *Nat. Geosci.* 7, 219–223.

804 Vance D., Müller W., Villa I.M., 2003. Geochronology: linking the isotopic record with petrology and textures - an
805 introduction. In: Vance D., Müller W., Villa I.M. (eds) *Geochronology: linking the isotopic record with petrology*
806 *and textures*. Geological Society London Special Publications, 220, 1-24.

807 Villa I.M. (1998) Isotopic closure. *Terra Nova*, 10,42-47

808 Villa I.M. (2010) - Disequilibrium Textures vs Equilibrium Modelling: Geochronology at the Crossroads. In: Spalla
809 M.I., Marotta A.M., Gosso G. (eds) *Advances in interpretation of geological processes*. Geological Society London
810 Special Publications, 332, 1-15.

811 Villa I.M. (2016) Diffusion in mineral geochronometers: Present and absent. *Chemical Geology*, 420, 1-10

812 Villa I.M. and Williams M.L. (2013) - Geochronology of metasomatic events. In: Harlov D.E., Austrheim H. (eds.),
813 *Metasomatism and the Chemical Transformation of Rock*. Springer, Heidelberg, 171-202. ISBN 978-3-642-28393-2.

814 Villa I.M., Bucher S., Bousquet R., Kleinhanns I.C. and Schmid S.M. (2014) Dating polygenetic metamorphic
815 assemblages along a transect through the Western Alps. *Journal of Petrology*, 55, 803-830

816 Villa I.M. and Hanchar J.M. (2017). Age discordance and mineralogy. *American Mineralogist*, 102, 2422–2439.

817 Wartho J.A., Kelley S.P., Brooker R.A., Carroll M.R., Villa I.M. and Lee M.R. (1999) Direct Ar diffusion
818 measurements in a gem-quality Madagascar K-feldspar using the Ultra-Violet Laser Ablation Microprobe
819 (UVLAMP). *Earth and Planetary Science Letters*, 170, 141-153

820 Wawrzenitz, N., Krohe, A., Rhede, D., Romer, R.L., (2012). Dating rock deformation with monazite: the impact of
821 dissolution precipitation creep. *Lithos* 132–135, 52–74.

822 Whitehouse M.J., Kusiak M.A., Wirth R. and Ravindra Kumar, G.R. (2017) Metallic Pb nanospheres in ultra-high
823 temperature metamorphosed zircon from southern India. *Mineralogy and Petrology* 111, 467–474

824 Williams, M.L., Jercinovic, M.J. (2002). Microprobe monazite geochronology: putting absolute time into
825 microstructural analysis. *J. Struct. Geol.* 24, 1013–1028.

826 Williams ML, Jercinovic MJ, Terry M (1999) High resolution « age » mapping, chemical analysis, and chemical dating
827 of monazite using the electron microprobe : a new tool for tectonic analysis. *Geology* 27: 1023-26

828 Williams ML, Jercinovic MJ, Hetherington CJ (2007) Microprobe monazite geochronology: understanding geologic
829 processes by integrating composition and chronology. *Annual Review of Earth Planet Sci Letters* 35:137–175.

830 Williams ML, Jercinovic MJ, Harlov DE, Budzyń B, Hetherington CJ (2011) Resetting monazite ages during fluid-
831 related alteration. *Chem Geol* 283:218–225

832 Williams M.L., Jercinovic M.J., Mahan K.H. and Dumond G. (2017) Electron Microprobe Petrochronology. *Reviews*
833 *in Mineralogy and Geochemistry* 83, 153-182

834 Zhu XK, O'Nions RK (1999) Zonation of monazite in metamorphic rocks and its implications for high temperature
835 thermochronology: a case study from the Lewisian terrain. *Earth Planet. Sci. Lett.* 171:209–220.

836

837

838

839

840

841

842

843

844

845

846

847

848

849

850

851

852

853

854

855

856

857

858

859

860

861

862

863

864

865

866

867

868

869

870

871

872

873

874

875

876

877

878

879

880

881

882

883

884

885

886

887

888

889

890

891

892

893

Figure Captions

1. Arrhenius diagram showing diffusion coefficients for garnet (Chakraborty and Ganguly, 1992) and monazite (Cherniak et al. 2004).
2. Different types of monazite zonations (EPMA X ray maps). (Didier et al. 2014; Didier et al. 2015; Bosse et al. 2009). (b) NanoSIMS distribution maps (^{89}Y , ^{139}La , ^{238}U , ^{208}Pb , ^{232}Th and $^{208}\text{Pb}/^{232}\text{Th}$), RGB maps (Y in *red*, Th in *green* and U in *blue*) and interpretive sketches of selected portions of Monazite. The sketches distinguish between the M1 (*red*), M2 (*green*) and M3 (*orange*) domains corresponding to successive monazite growth stages. Didier et al. (2015)
3. Inverse relation between assumed "closure temperature" and age of peak metamorphism in a traverse across the Central Alps. The x axis is eastings, for convenience indicated as peak metamorphic temperature. (a) By assuming an excessively low retentivity of $^{87}\text{Sr}^*$ in muscovite (dashed), monazite (solid line) is inferred to record cooling below ca. 450 °C (redrawn after Steck and Hunziker 1994). (b) By assuming that monazite always dates its own crystallization, and thus the metamorphic peak, most muscovite samples record isotopic inheritance of $^{87}\text{Sr}^*$ even at 650 °C. The tectonic implications are far-reaching: the exhumation rates and differential movements of the tectonic units in (b) is radically different from the incorrect ones in (a), which means that the starting assumption was incorrect.
4. Mineral ages in monometamorphic sediments in the Central Alps (data from Allaz et al. 2011). Peak metamorphism for rock AMo0410 is followed by paragonite destabilization, consumption of the first paragonite generation (Prg-1), and then growth of a Prg-2 after the rock re-entered the paragonite stability field during exhumation. The biotite age lies between the peak age and the age of Prg-2, and corresponds to the sum of chloritization and pure retrogression-free diffusion.
5. Thermochronology vs petrochronology of white mica in a traverse across the Western Alps (data from Villa et al. 2014). (a) Thermochronological prediction: the ages of detrital micas remain high until the "closure temperature" (here shown as 375-400 °C) is reached, then decrease continuously as peak temperatures increase. (b) Observation: the data-points (black circles) demonstrate Ar loss at $T < 300$ °C, complete Ar retention at 600 °C, and correlated exchange of Ar and Si at intermediate T. The Ar retention behaves asymptotically, as phengite ages do not become younger as peak temperature increases, but instead remain constant and equal to the Lu-Hf garnet ages. The predictions of thermochronology are all violated, which means that the thermochronologically inferred tectonic history (Cretaceous eclogitization, discrete greenschist event, delayed exhumation) are all incorrect.

Fig. 6 - Alteration experiments on natural monazite crystals under alkali conditions at 400 (A), 500 (B) and 600 (C) °C and 200 MPa (Grand'Homme et al. 2016). A,B, C: Transmission electron microscope images in bright field mode (BF-TEM) from focused ion beam (FIB) foils prepared at the reaction interface of experimental products; D: Energy-dispersive spectroscopy spectrum obtained on primary monazite (Mnz1) and secondary monazite (Mnz2) domains at 500 °C.

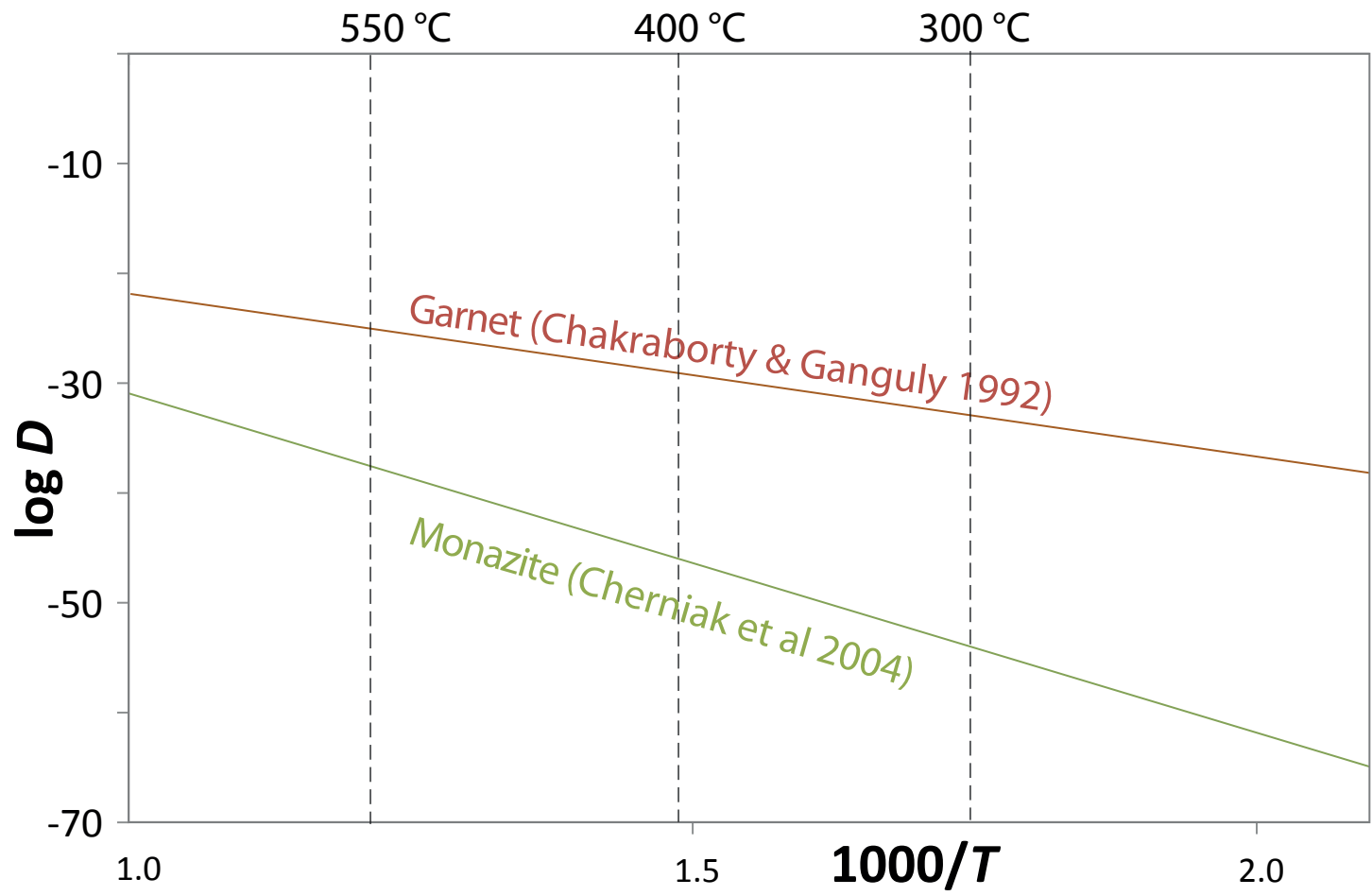
Fig. 7 - Tera-Wasserburg diagram of analyses for single grains of altered monazite (filled ellipses), ~~in~~ altered monazite affected by Pb loss (dashed ellipses), pristine monazite and an inherited monazite (empty ellipses) from the Montasset microgranite. Upper inset: $^{208}\text{Pb}/^{232}\text{Th}$ age probability histogram for all altered monazite grains; Right inset: X-ray Th element map of a hydrothermal monazite grain (Didier et al. 2013)

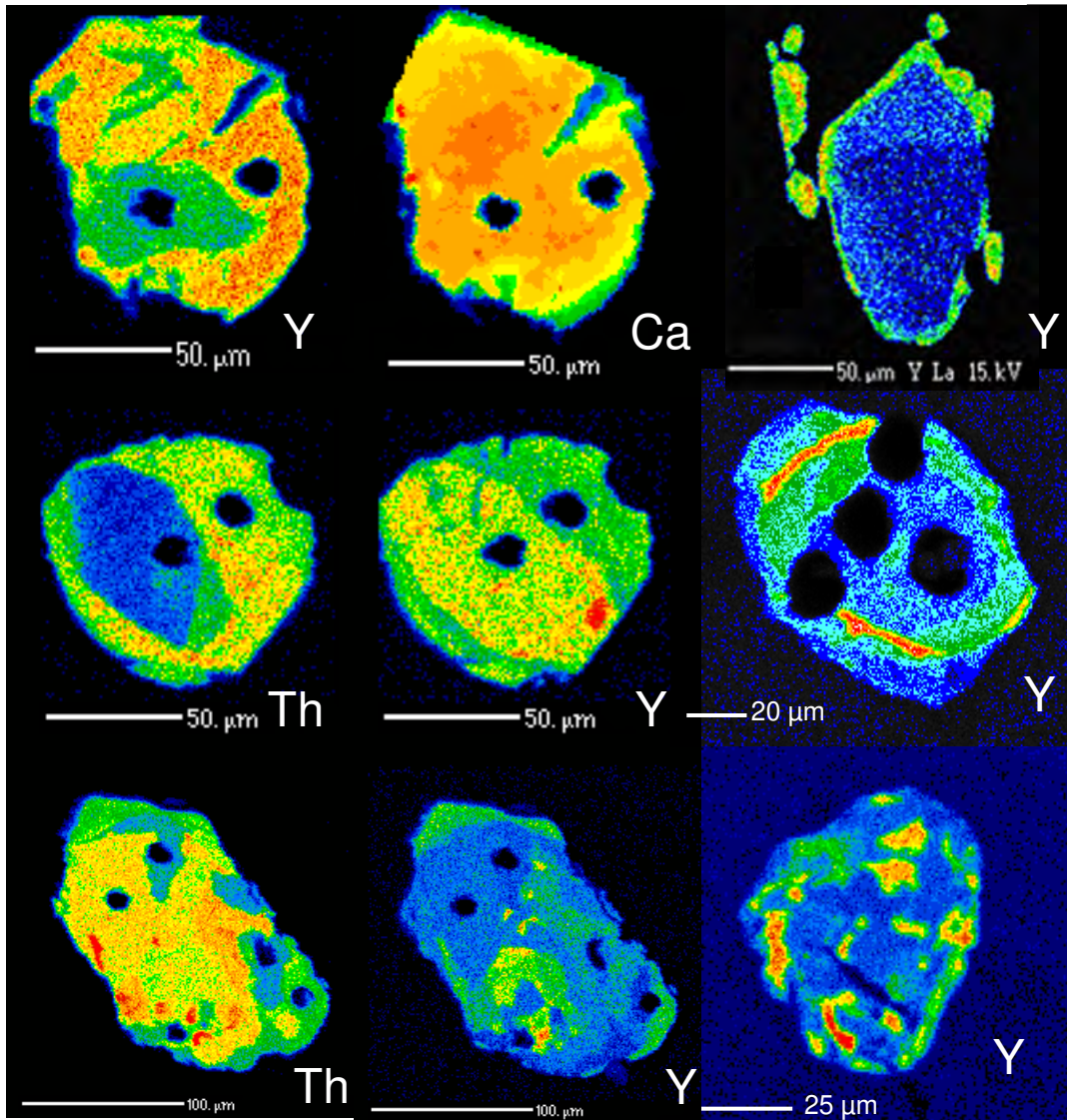
Fig. 8 - BSE images of monazite from the Rhodope Grt-Ky metapelites showing evidences of syn-deformation fluid-assisted monazite growth (Didier et al. 2014).

Fig. 9 - BSE images and yttrium X-ray maps of matrix monazites in the Rhodope Grt-Ky metapelites (Didier et al. 2014). Circles show the location of the LA-ICPMS pits (11 μm) and their corresponding $^{208}\text{Pb}/^{232}\text{Th}$ ages (green and orange : concordant ages, white : mixing ages; 2σ uncertainty).

Fig. 10 - Monazite textures in eclogite-facies gneiss from the Les Essarts HP unit (Southern Armorican Massif, France): **Left** : apatite, zoisite and monazite (Mnz 2) developed at contacts between primary monazite (Mnz 1) and plagioclase; kaolinite (Kln) probably results from the late alteration of metamict plagioclase. Image obtained from X-ray element maps, after phase classification (Godard, 2009); **Right** :

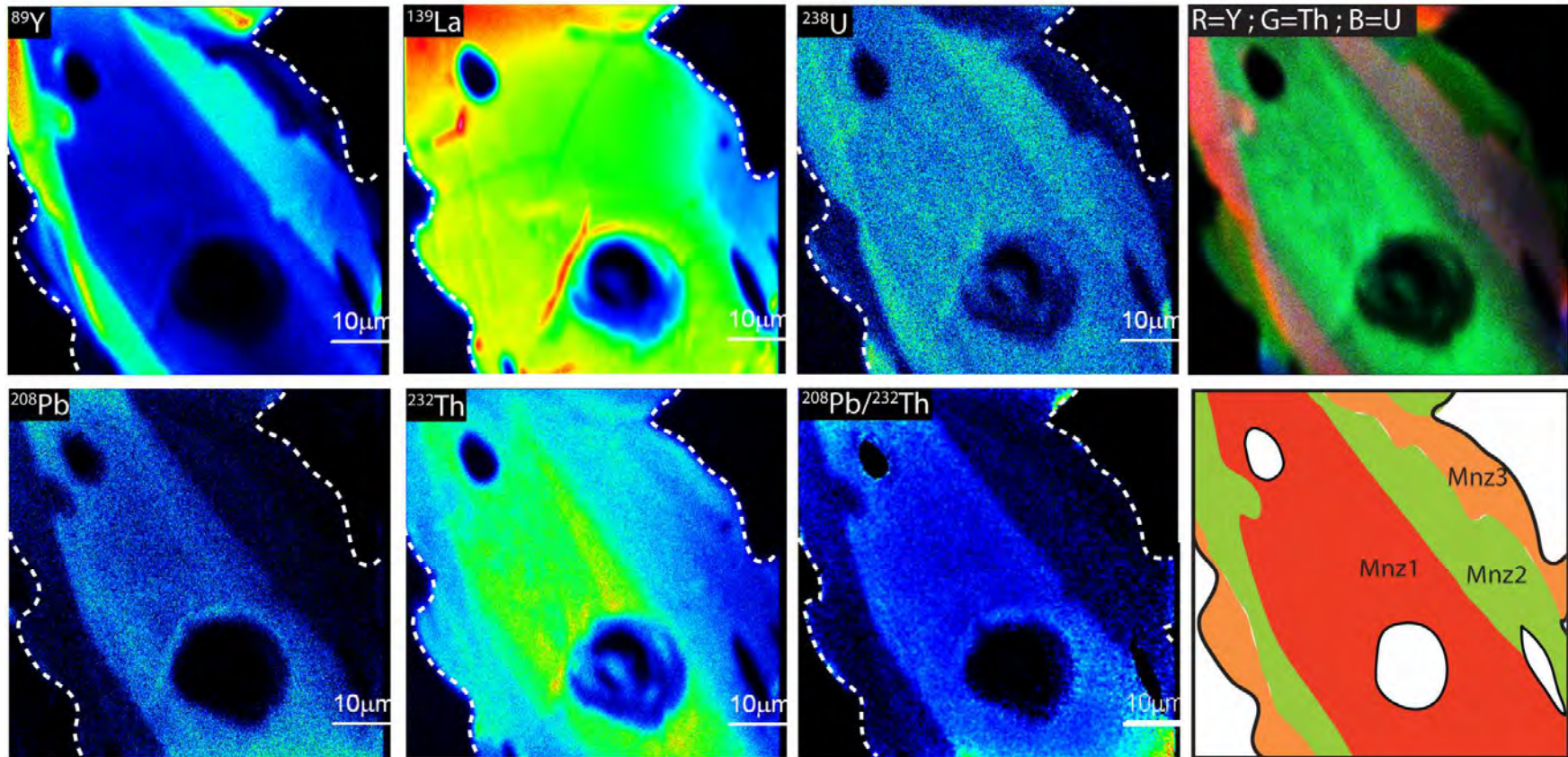
894 BSE image and corresponding LA-ICPMS $^{208}\text{Pb}/^{232}\text{Th}$ ages (spot size $5\mu\text{m}$, 2σ uncertainty) (Bosse et
895 al. 2010)
896 Fig. 10 - Summary of the petrochronological results (P–T paths and monazite $^{208}\text{Pb}/^{232}\text{Th}$ ages). Note the
897 presence of HP inclusions, which confirm the crystallization of the monazite during HP metamorphism
898 conditions. Money Units (a) and Gran Paradiso (b), modified after Manzotti et al. (2018).
899





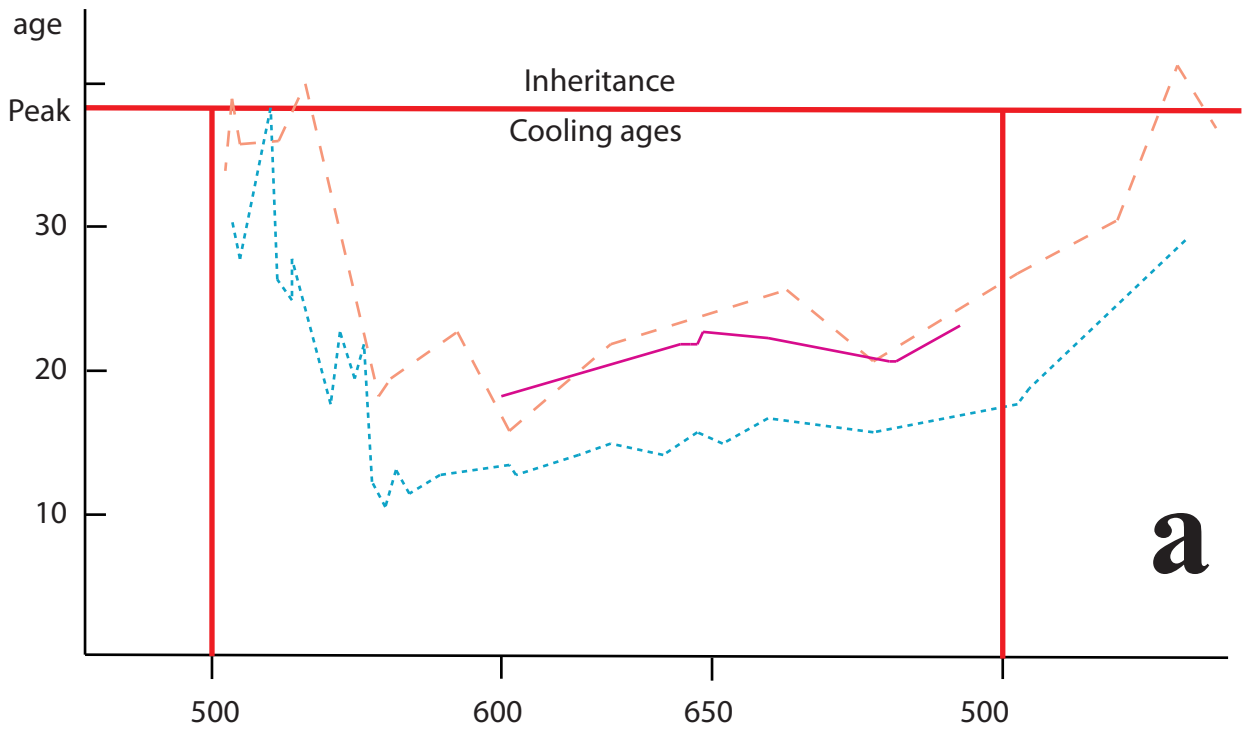
Different types of monazite zonation (EMP X ray maps). (Didier et al. 2014; Didier et al. 2015; Bosse et al. 2009)

Fig. 2a

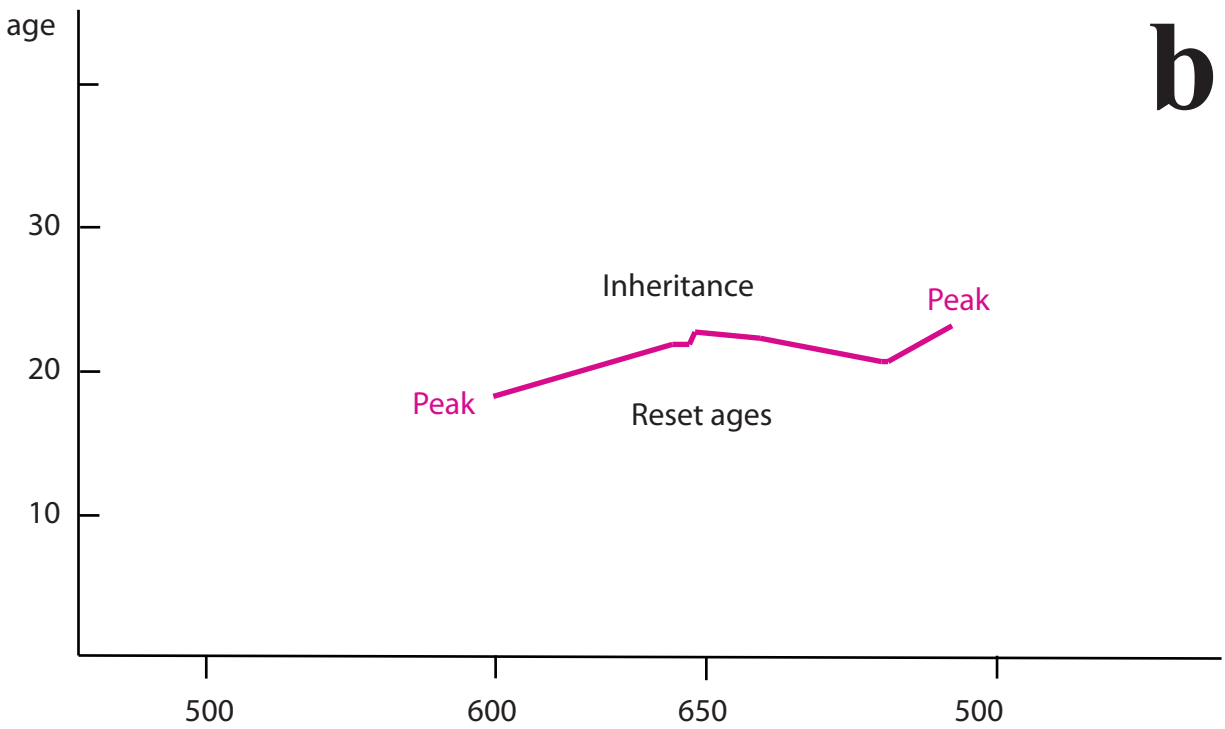


NanoSIMS distribution maps (^{89}Y , ^{139}La , ^{238}U , ^{208}Pb , ^{232}Th and $^{208}\text{Pb}/^{232}\text{Th}$), RGB maps (Y in red, Th in green and U in blue) and interpretive sketches of selected portions of Monazite. The sketches distinguish between the M1 (red), M2 (green) and M3 (orange) domains. Didier et al. (2015)

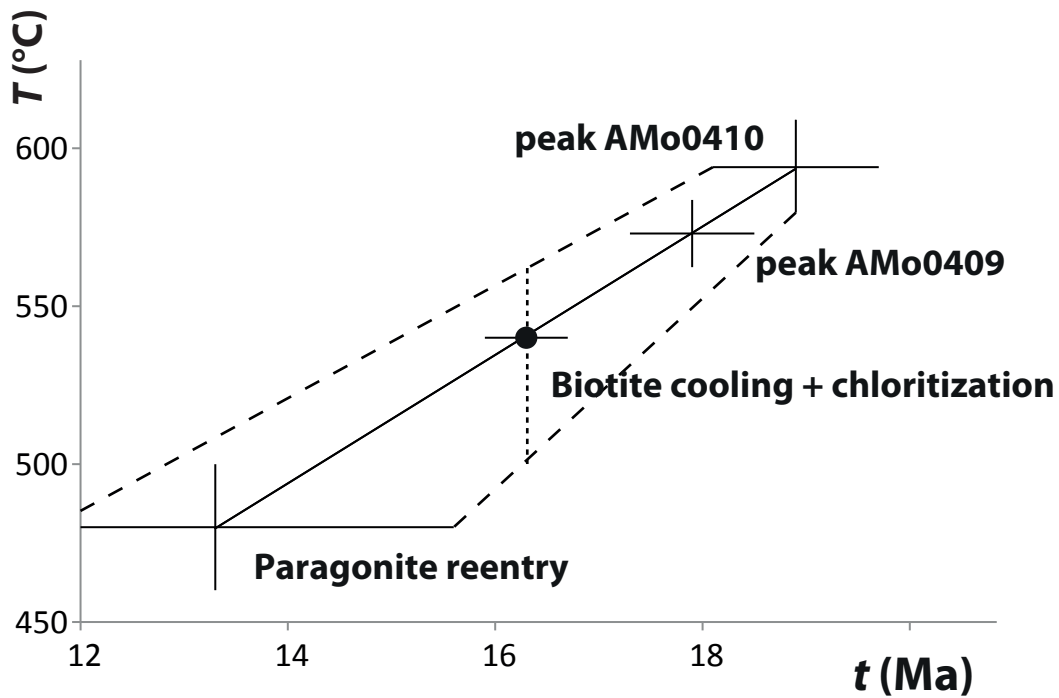
Fig. 2b



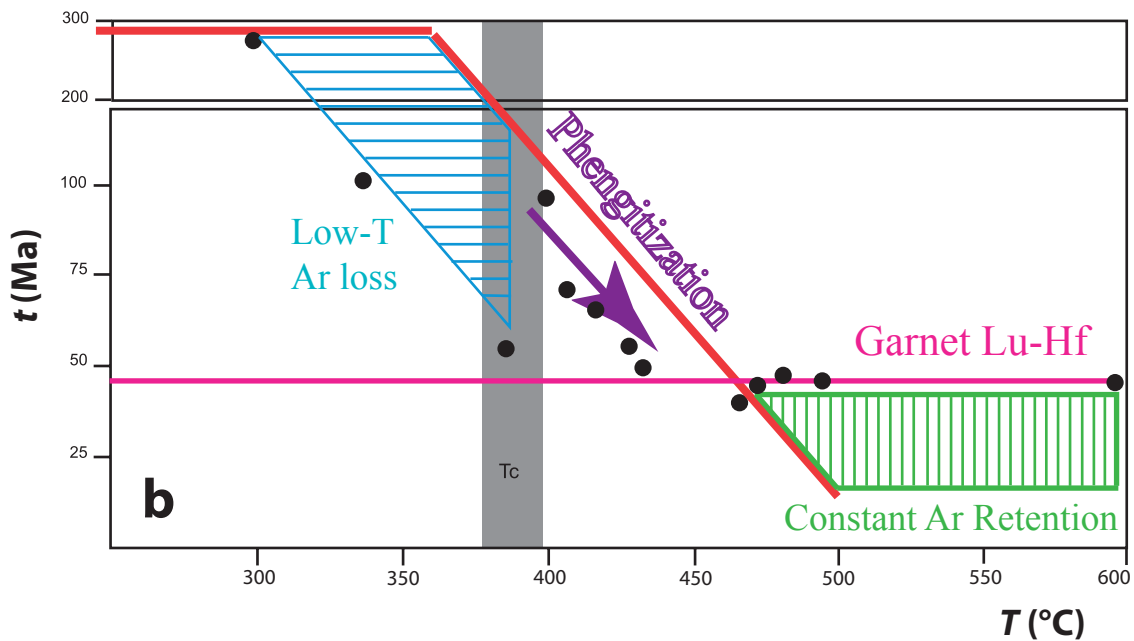
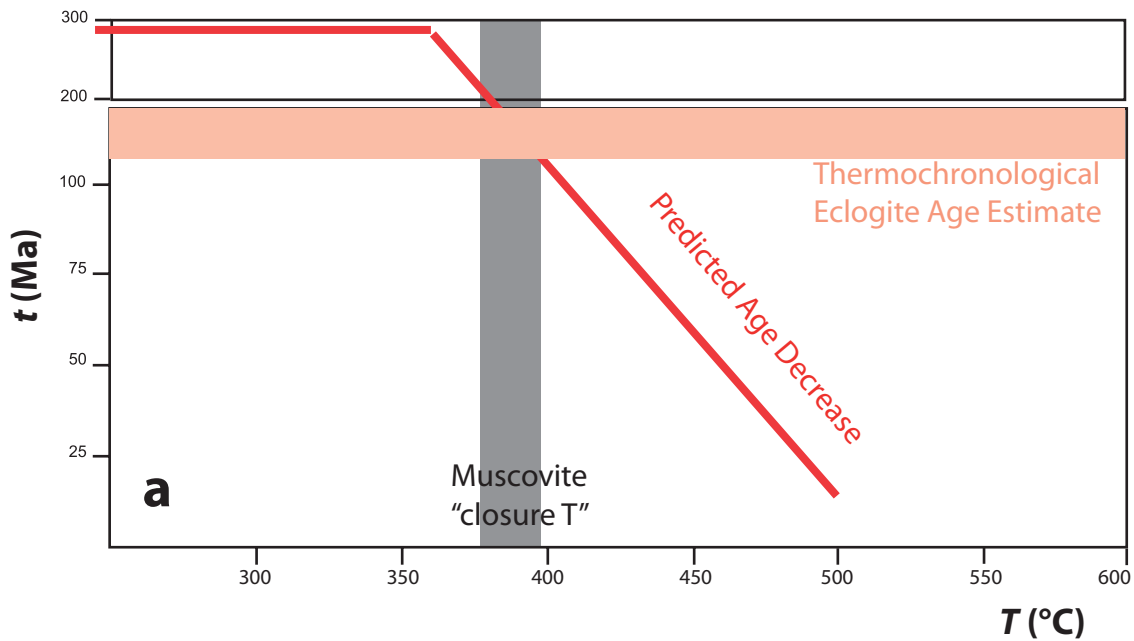
a



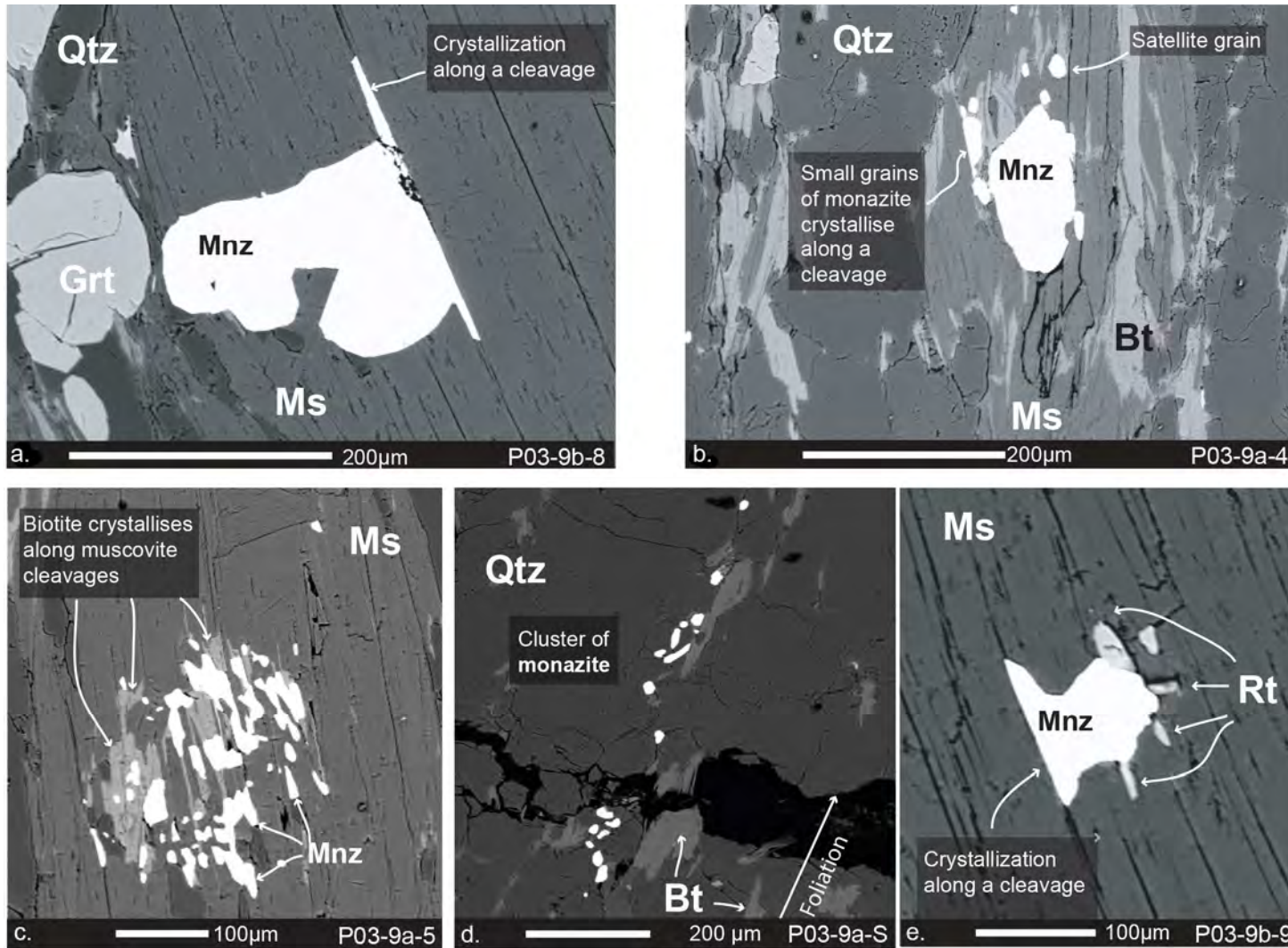
b



Bosse&Villa - Fig. 3

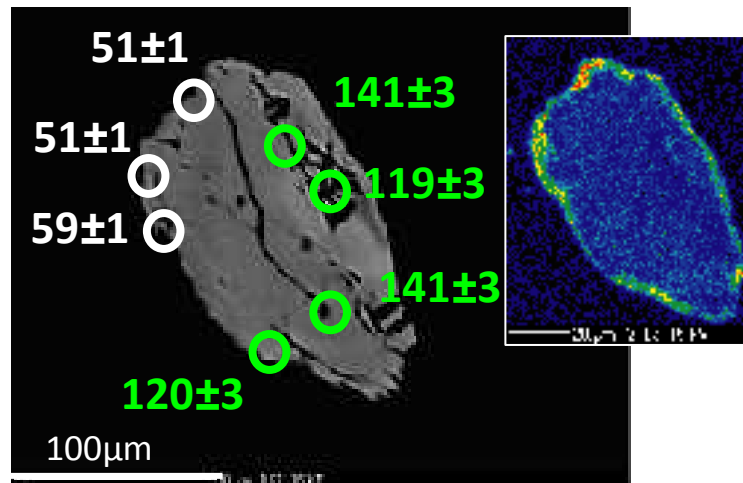
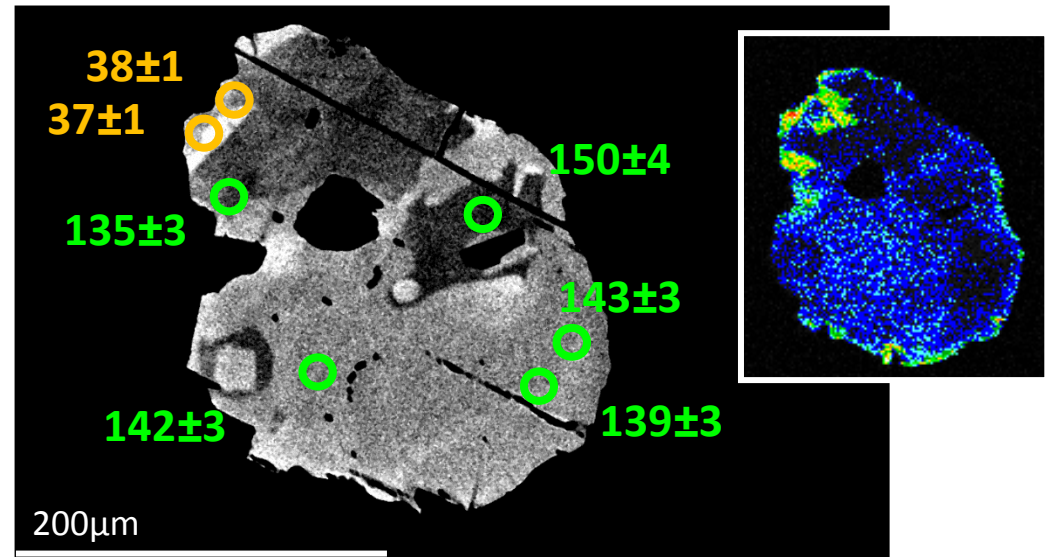
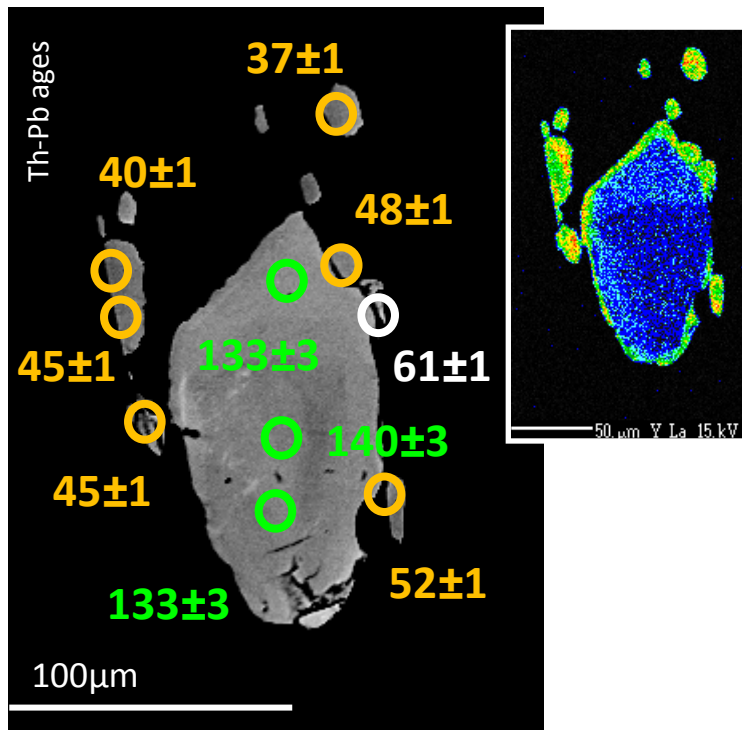


Bosse & Villa - Fig.



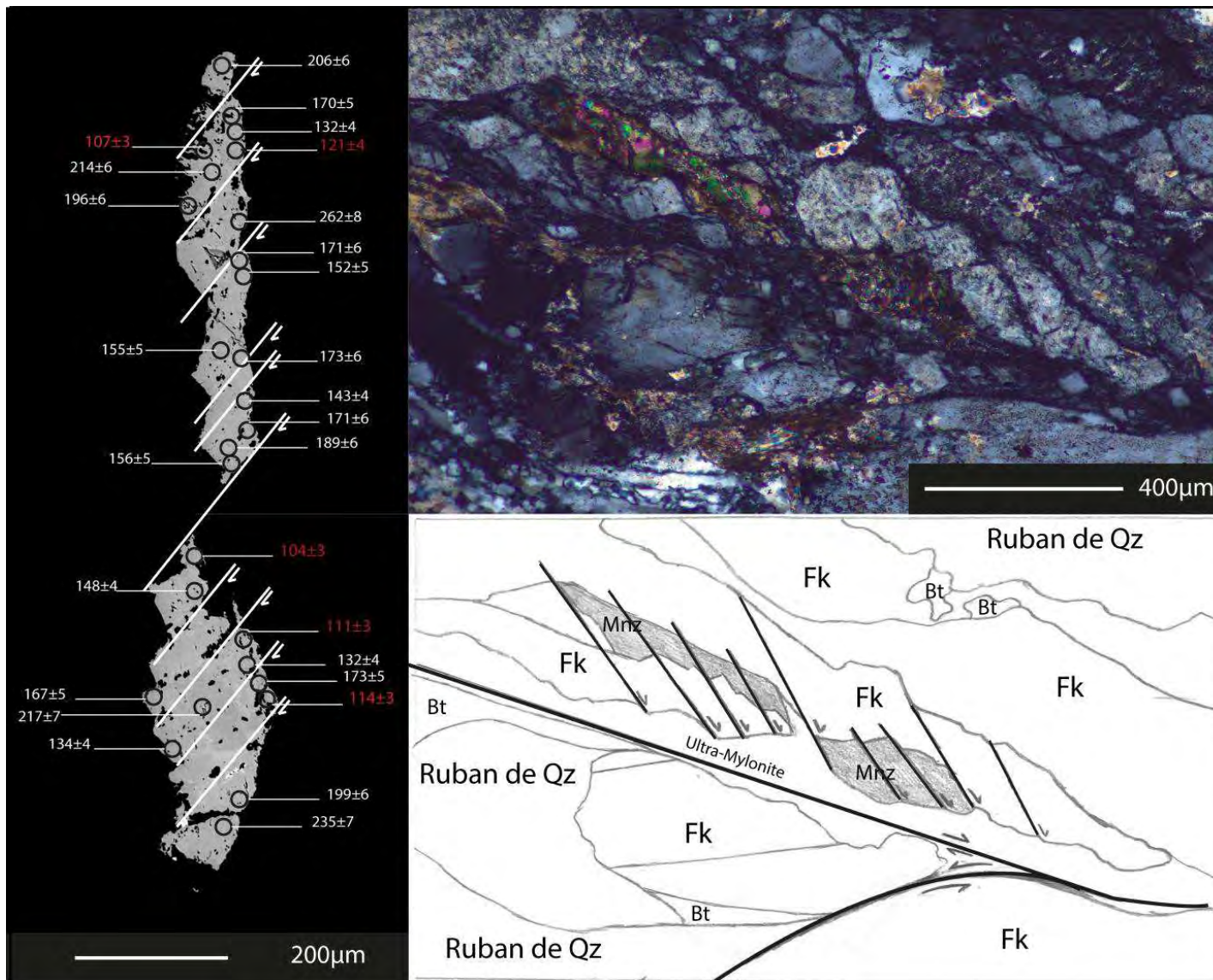
BSE images of monazite from the Rhodope samples (Didier et al. 2014) showing evidences of syn-deformation fluid-assisted monazite growth

Fig. 3



BSE images and Y X-ray maps of matrix monazites in the Rhodope samples (Didier et al. 2014) Circles show the location of the LA-ICPMS pits (11 µm) and their corresponding $^{208}\text{Pb}/^{232}\text{Th}$ ages (2σ level).

Fig. 4



BSE image with $^{232}\text{Th}/^{208}\text{Pb}$ ages (spot size $7\mu\text{m}$). In red, concordant ages and in white mixing (meaningless) ages. Right : Photomicrograph of the monazite texture and sketch showing the deformation.

Fig. 5

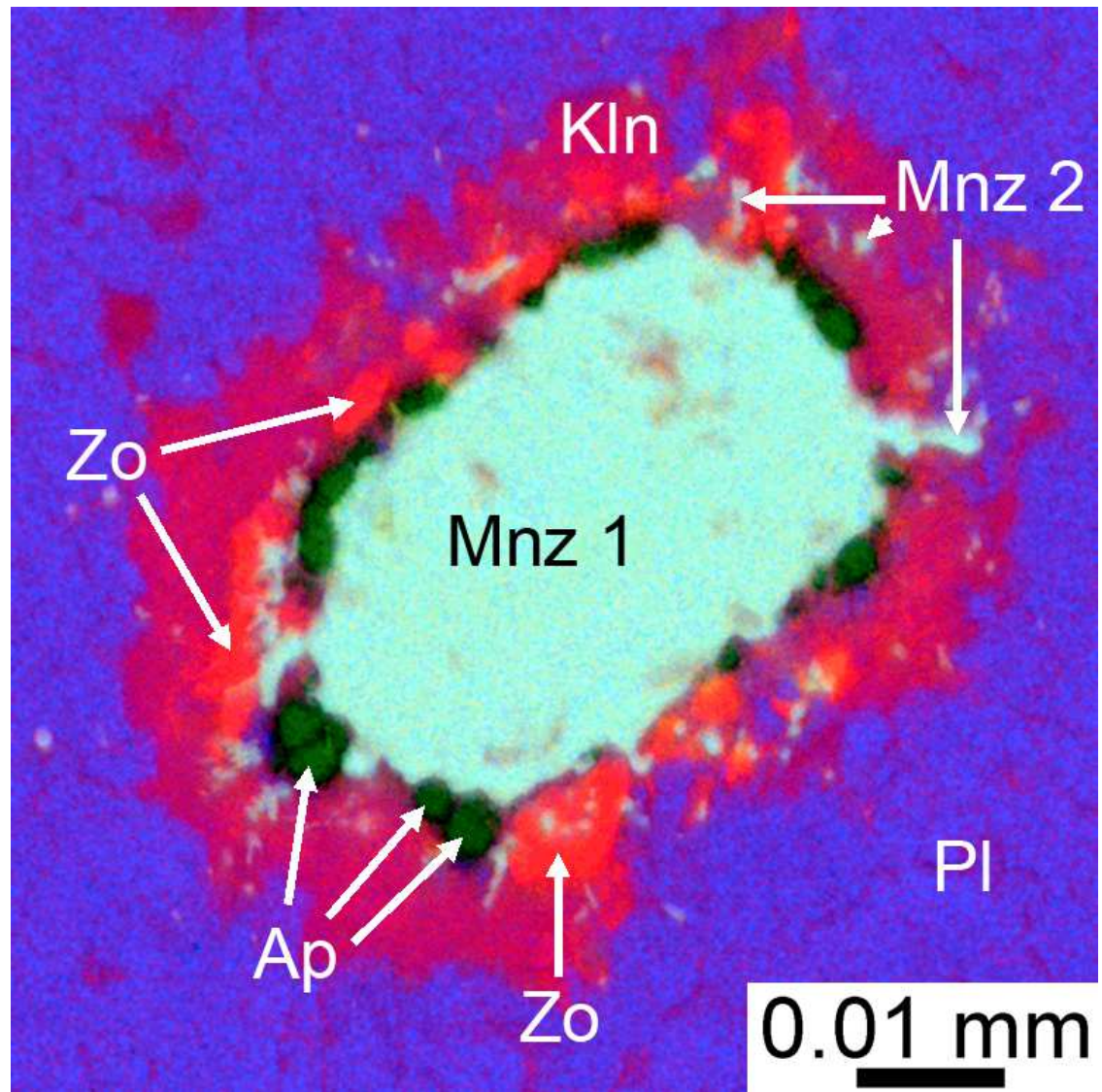
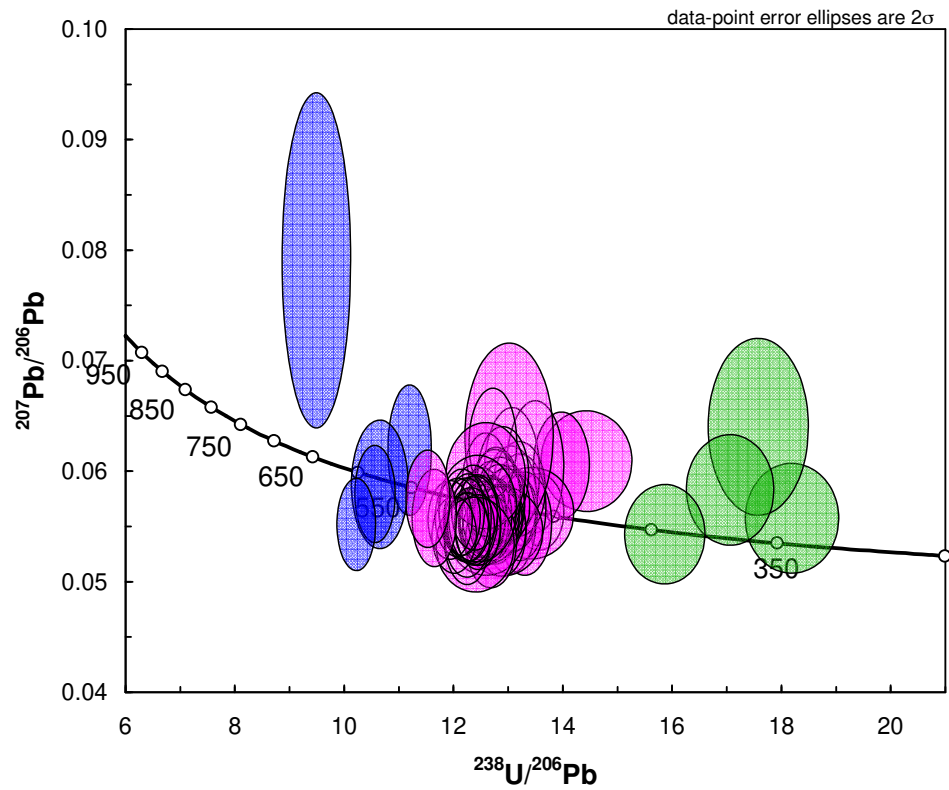
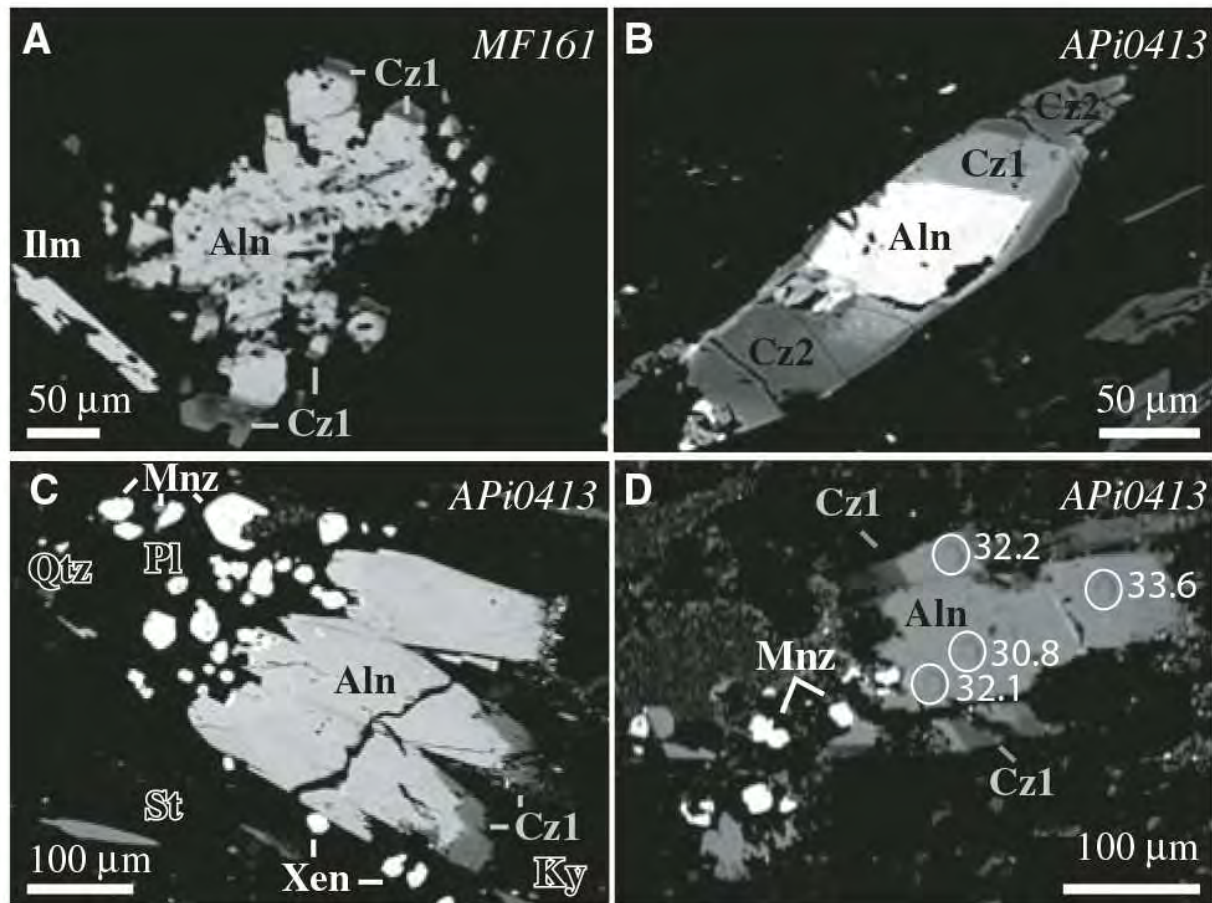


Fig. 6



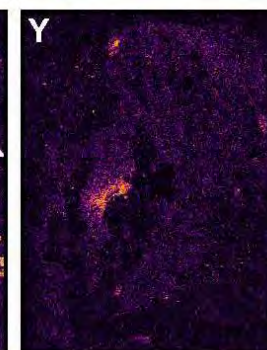
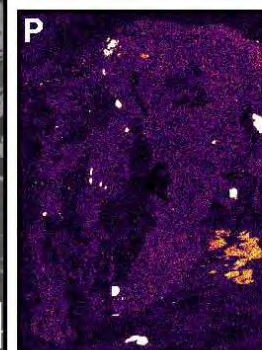
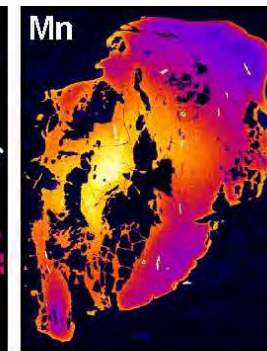
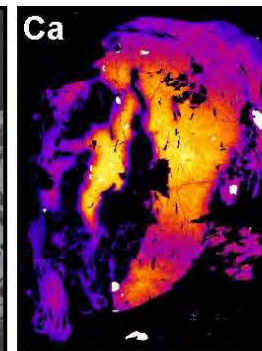
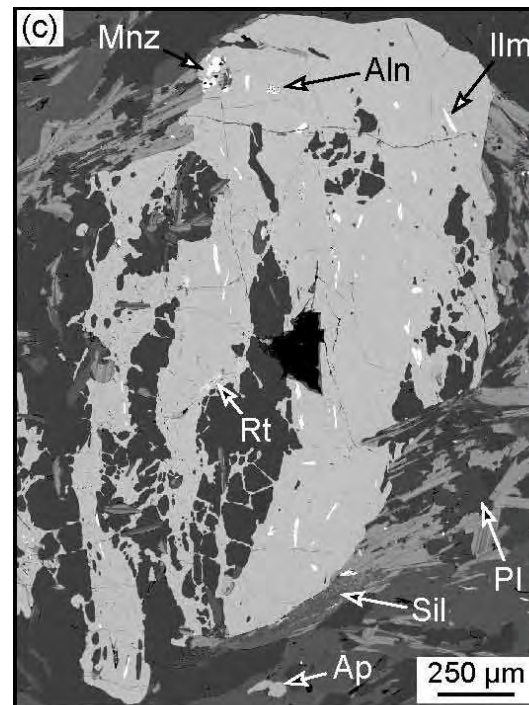
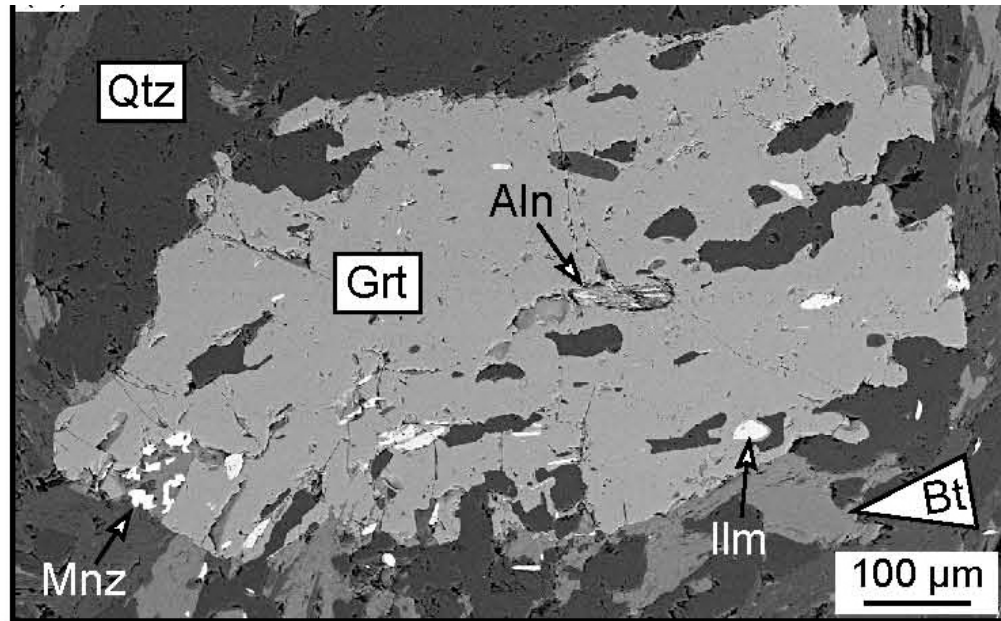
To be improved ...

Tera Wasserburg diagram showing the three monazite generations recorded in the Vendée paragneisses (Bosse et al. 2010)



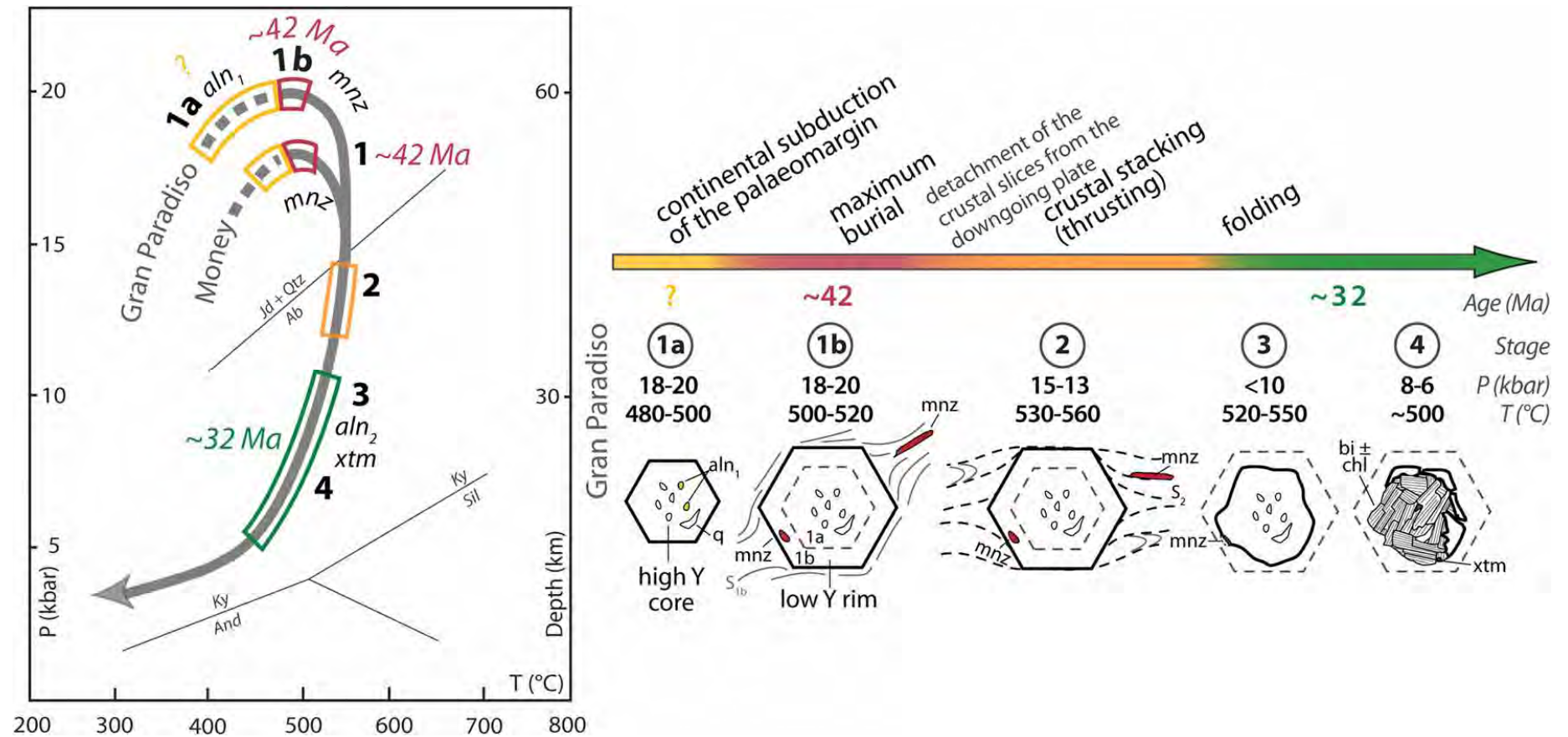
Janots et al. 2009...

Fig. 8



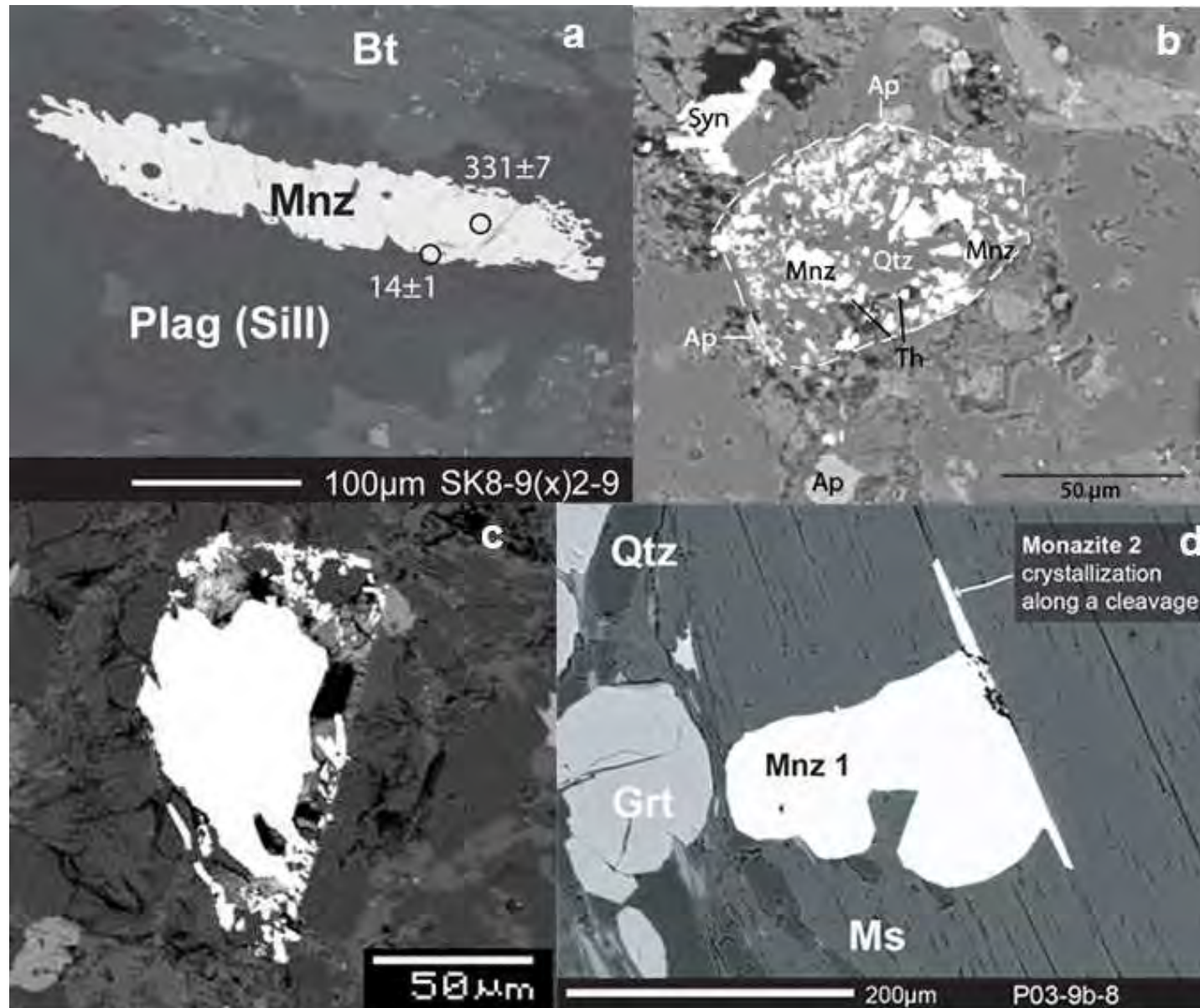
Skrzypek et al. 2016...

Fig. 9



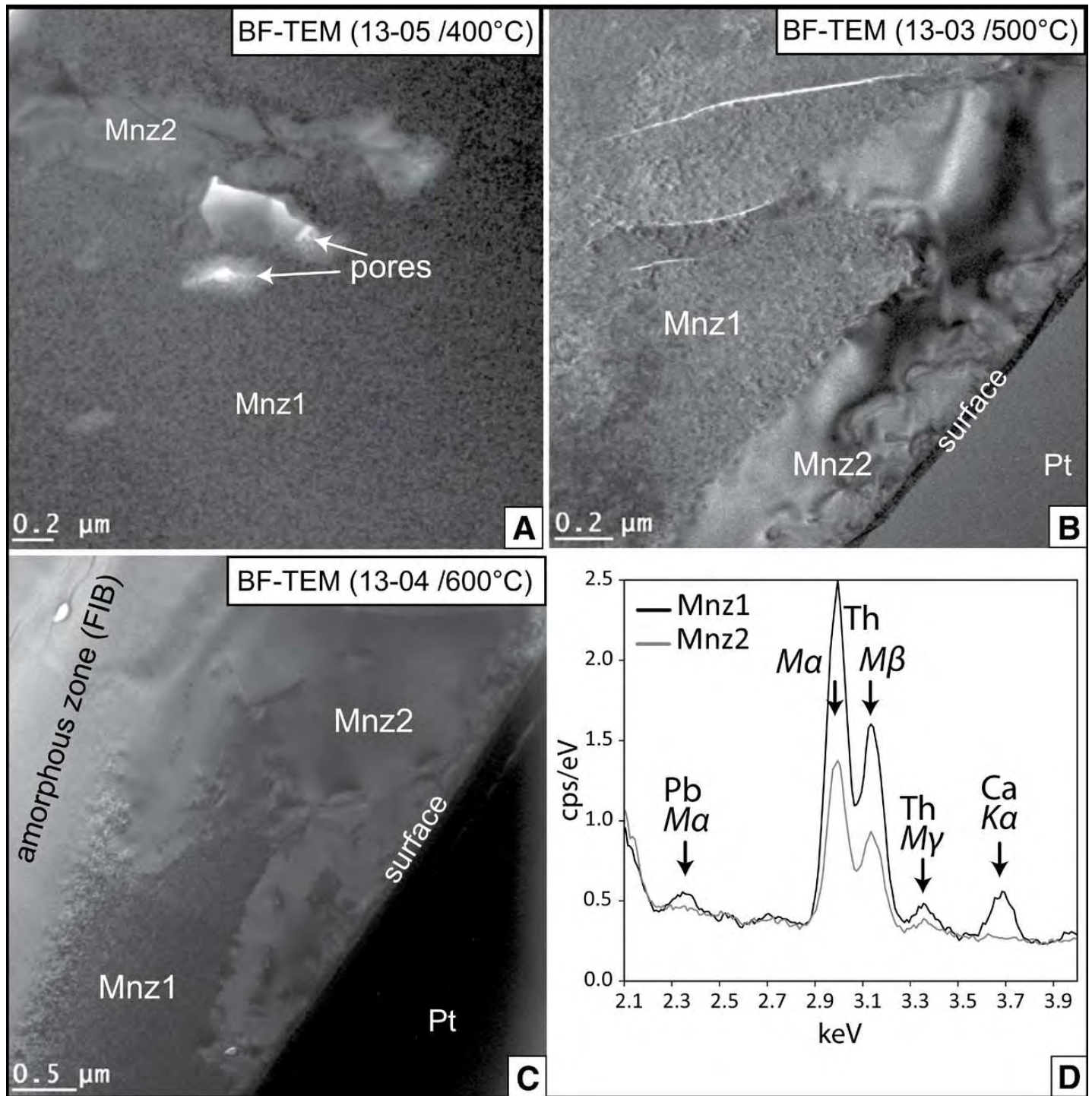
Summary of the petrochronological results (P - T paths and monazite, allanite and xenotime ages) for the Gran Paradiso and Money Units (Manzotti et al. 2018)

Fig. 10



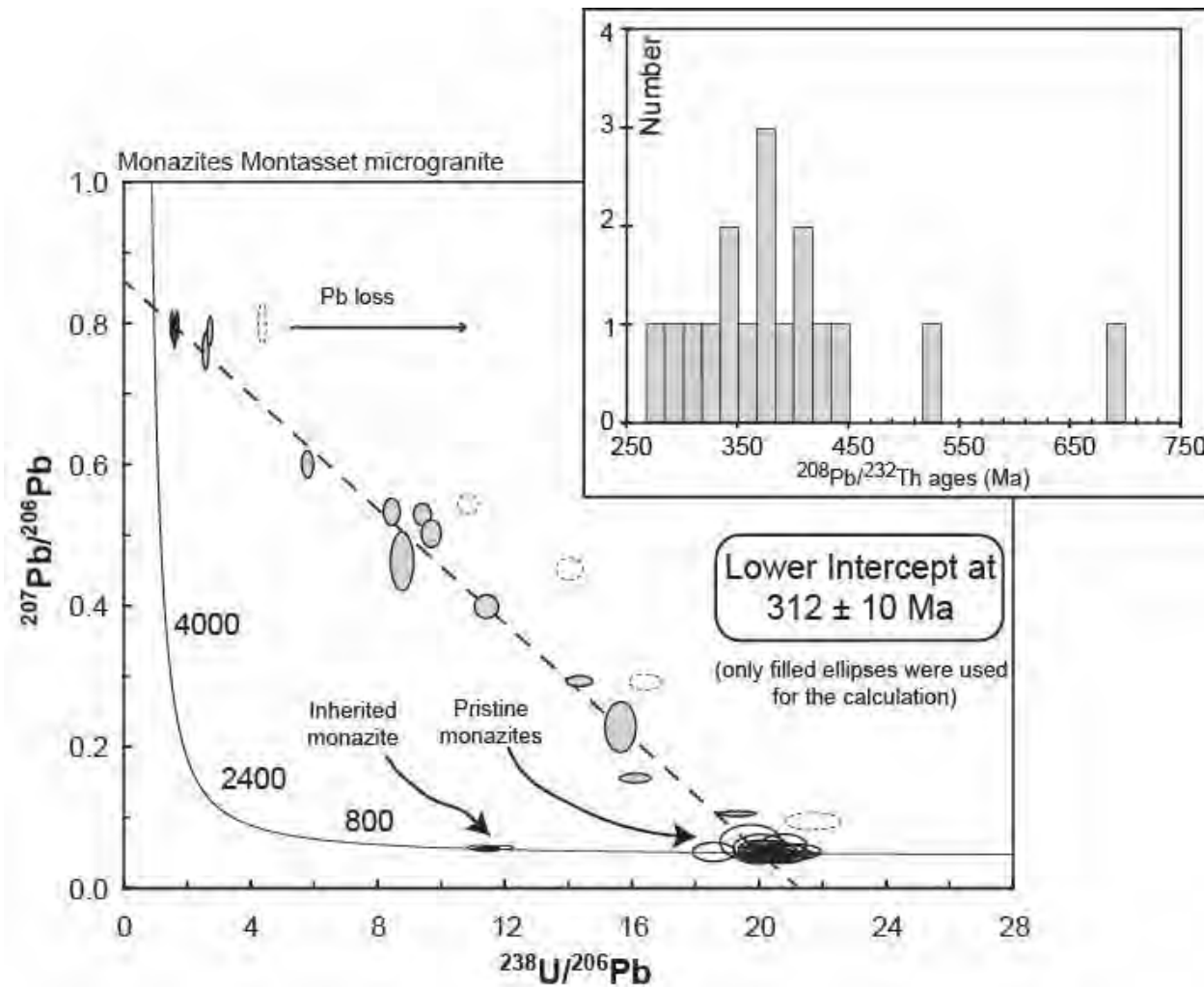
To be modified...

Fig. 11



Grand'Homme et al. 2016

Fig. 12



Tera–Wasserburg diagram of analyses in altered monazites (filled ellipses), in altered monazites affected by Pb loss (dashed ellipses), pristine monazites and an inherited monazite (empty ellipses) from the Montasset microgranite. Only altered monazites (filled ellipses) were used to calculate the U–Pb age at $312 \pm 10 \text{ Ma}$. In the right corner: $^{208}\text{Pb}/^{232}\text{Th}$ age probability histogram for all altered monazites (Didier et al. 2013)